

Global modelling of heat transfer in crystal growth furnaces

F. DUPRET, P. NICODÈME, Y. RYCKMANS, P. WOUTERS and
M. J. CRÖCHET

Unité de Mécanique Appliquée, Université Catholique de Louvain, Place du Levant, 2,
B-1348 Louvain-la-Neuve, Belgium

(Received 7 April 1989)

Abstract—A quantitative prediction of the thermal field and the location of the melt-crystal interface during growth requires a precise knowledge of the heat transfer taking place in the entire furnace. The problem is highly complex since it involves an accurate calculation of radiation between the different surfaces and conduction in the constituents. Radiative exchanges are calculated with the assumption of diffusive surfaces and with use of a viewed and hidden part algorithm together with a Galerkin discretization. The model has been extended for taking semi-transparent materials into account. The shape of the liquid-solid interface is a variable of the problem and is calculated as being the melting isotherm. Examples of germanium and gallium arsenide furnaces are analysed, showing the efficiency of the method.

1. INTRODUCTION

MOST SEMICONDUCTOR crystals are grown in Czochralski pullers, in which a cylindrical crystal is pulled from the surface of the melt. Gallium arsenide and indium phosphide crystals are usually grown with the LEC (liquid-encapsulated Czochralski) process. The calculation of heat transfer in such furnaces is complex in view of the strong coupling between diffusive, advective and radiative exchanges. A review of the various aspects affecting heat transfer in a Czochralski furnace may be found in ref. [1]. Over the last four years, a major effort has been accomplished for considering the whole furnace as a system where the growth of the crystal is simulated on the basis of a reduced number of controllable parameters, such as the power input in the heater, the coolant temperature, the pulling rate and the diameter of the crystal. In a series of papers, Derby *et al.* [2-6] developed a simplified model of the furnace radiating towards an ambient temperature. They studied the dynamics of the growth process and its control, and considered the variation of the crystal radius during growth. A more elaborate thermal model taking into account radiative exchanges between the various constituents was later elaborated by Atherton *et al.* [7], but the ambient temperature on the outer walls was still part of the data. In an earlier paper, Srivastava *et al.* [8] had also used a radiative model on a reduced geometry, with an analytical calculation of the view factors. More recently, Motakef and Witt [9] and Motakef [10, 11] developed a thermal model which is very similar to that in ref. [7], except that the radius of the crystal is uniform.

In these various papers, a certain degree of indeterminacy is left on the distant surfaces such as the wall of the furnace or the bottom plate; the effect of

including additional components in the heater, such as reflectors above the crucible, is not straightforward.

In the present paper, we wish to pursue the analysis initiated by Wouters [12]. The method has briefly been reviewed in ref. [13], where we described a heat transfer model of the furnace which is self-contained; input parameters other than the coolant temperature and the power input—or the pulling rate—are not required, provided the complete geometry (including the uniform radius of the crystal) is fully characterized. Since the publication of refs. [12, 13], the method has been refined and several practical applications have been published [14-17]. In what follows, we wish to give a complete description of the thermal model and the numerical method used in these papers.

A major ingredient of the model is the calculation of the radiative transfer. Analytical methods were eliminated *a priori* in view of the geometrical complexity of common furnaces and the nonlinearity of the problem. A first numerical approach would be the Monte Carlo method, which lies on a statistical basis [18, 19]. Such a method is well adapted for solving complex problems, but it has not been retained in view of its high cost for a sufficient accuracy. A second approach is the net-radiation method; when the latter is combined with zonal analysis [20-23], the surface of the enclosure is divided into a number of isothermal patches, while radiative transfer is calculated between every pair of such patches. First, one calculates the configuration (or view) factor associated with every pair, while taking into account the viewed and hidden parts of the enclosure. Matrix operations then provide the total-exchange areas (or the Gebhart factors) between the pairs; this means that successive reflections are now taken into account. The total-exchange areas produce the relationships between net fluxes and radiative emitted fluxes, i.e. the matrix relationship

between net fluxes and fourth powers of temperatures on the enclosure. Such an approach was followed by Atherton *et al.* [7], where circular cross-sections of the crucible are replaced by octagons.

In our work, we have taken full account of the circular symmetry of the furnace. The temperature field on the enclosure is represented by means of quadratic one-dimensional finite elements. Galerkin's method [24] is used for solving the radiative integral equation; it leads to a high accuracy which is closely related to that of the numerical integration. Let us in particular emphasize the importance of radiative exchange near the tri-junction, where the crystal meets the melt. View factors between infinitesimal conical surfaces are calculated analytically by means of an original method which is equivalent to but differs from Garot and Gendre's method [25]. A major advantage of our algorithm is that the full analysis is performed in a planar cross-section of the furnace, and is thus an appropriate tool for furnace design.

A study of the LEC growth requires to take into account the presence of a semi-transparent oxide layer. While the limit cases of transparency and opacity are studied in ref. [10], we have applied the band-energy method [19], considering that the layer is transparent for some ranges of wavelengths and opaque for others. We will find that the transparency coefficient has important implications upon the temperature distribution and the thermal stresses.

A significant problem of using semiconductors for high quality electronic substrates is the presence of dislocations. They are usually related to thermal stresses [26, 27] generated during growth which, beyond a critical level, give rise to plastic deformations. Thus, a common way of estimating the density of dislocations, at least on a qualitative basis, has been to calculate thermal stresses during growth. Analytical methods have been used by Kobayashi and Iwaki [28] and Jordan *et al.* [29, 30], while Duseaux [31] used a finite element method for this purpose. In such studies, the thermal boundary conditions on the crystal are selected at the outset and take little account of the surrounding ambience and of the shape of the interface. An examination of thermal stress contours shows however that an accurate evaluation of such stresses requires in turn an accurate description of the temperature field. Methods based on measured temperatures [32] lose the predictive power which is desired for modifying the geometry of the furnace. An analysis of the thermal stresses on the basis of a global heat transfer analysis has been developed by Motakef and Witt [9] and Motakef [10, 11]. Similarly, a finite element prediction of thermal stresses is coupled to our global heat transfer calculation. For this reason, our model is a powerful tool for acting on the magnitude of the temperature gradients in order to decrease the dislocation density (or the thermal stresses) [14, 16].

At this stage, we have not mentioned the motion of the melt caused by natural and forced convection.

Although advective phenomena have been taken into account in our earlier publications [15, 17, 33], we have not included their description in the present paper for the sake of brevity. It should be recalled that the low Prandtl number characterizing metallic melts reduces the influence of convection on the temperature field, particularly in the case of germanium growth.

Since our goal here is to present the method for calculating heat transfer in the furnace, the paper is organized along the basic steps of the algorithm. Having introduced definitions and basic hypotheses in Section 2, we present our algorithm for radiative enclosures in Section 3. Heat conduction is studied in Section 4, while the solid-liquid interface is examined in Section 5. In Section 6 we elaborate on the important topic of selecting a strategy for solving the global system of non-linear equations; in particular, we discuss whether one should impose the power input or the pulling rate. Having briefly recalled the calculation of thermal stresses in Section 7, we analyse two examples in Section 8, related to the growth of germanium and gallium arsenide crystals.

2. BASIC HYPOTHESES AND DEFINITIONS

The geometry of the global problem that we wish to solve is illustrated in Fig. 1, where the components of a typical Czochralski puller are shown which will

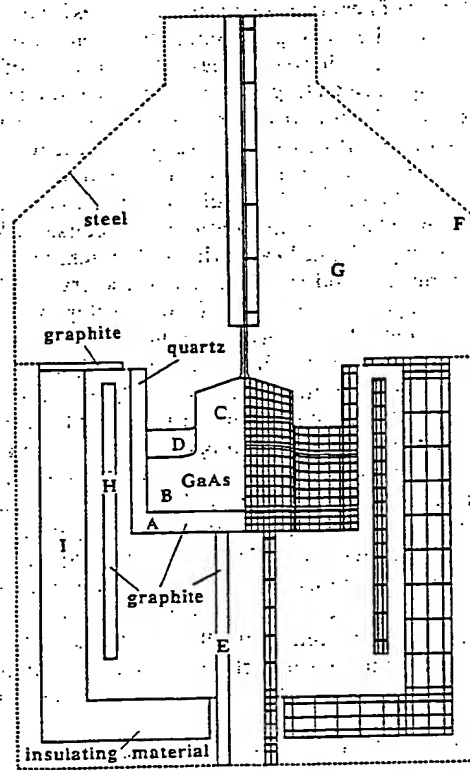


FIG. 1. Geometry of a typical LEC Czochralski puller and associate global finite element mesh.

serve as a basis for illustrating our method in later sections. We will assume at the outset that the geometry is axisymmetric. It may therefore be necessary to distribute in the azimuthal direction some parts of the furnace which are not symmetric, such as the wiring of the heater. In Fig. 1, the heater H radiates power towards the crucible A and the insulating wall I. The crucible A maintains the metal above the melting point; some heat is evacuated through the pedestal E. The crystal C is pulled from the melt B with a release of latent heat of fusion at the interface, while heat is transferred by conduction from B to C. The surfaces of the melt and of the crystal radiate heat inside the enclosure G towards the wall F which is cooled by water circulation. For the case of LEC growth, the melt is covered by a boric oxide layer D. The transfer of heat through D is a combination of conduction and radiation, since the oxide layer is semi-transparent to infra-red radiation. The semi-transparent property will be analysed in Section 3.

Our main interest is to calculate the shape of the liquid-solid interface and the temperature distribution within the crystal at various stages of its growth. It might therefore be sufficient to limit the domain of our calculations to the melt B and the crystal C. However, the temperature distribution in these components depends strongly upon the boundary conditions on their outer surface, which are a priori unknown. An accurate calculation of the temperature field will thus require a global calculation of the heat transfer throughout the whole furnace, on the basis of its geometry and its material properties, and a limited number of control parameters.

Our method is based on an idealized procedure where the crystal is grown with a constant radius selected at the outset. This would require an ideal control of the growth process; we generally calculate the power input while the growth rate is imposed. We also assume that the whole furnace is in a quasi-steady state [4], where one does not take into account the growth history of the crystal. More precisely, the time dependence of the geometry is not taken into account; however, for a fixed situation at a given time, the release of latent heat of fusion at the interface is proportional to the imposed growth rate. The quasi-steady hypothesis is valid since the time constants corresponding to geometrical modifications are much larger than the ones associated with heat transfer within the furnace.

In order to develop our mathematical model, we wish to separately consider four types of media within the furnace:

- (i) radiative enclosures which connect the various liquid and solid constituents;
- (ii) solid domains such as the heater, the crucible, the pedestal and other constituents where heat is transferred by conduction;
- (iii) outer thin walls cooled by external convection;
- (iv) the crystal and the melt together with their interface.

Briefly, the global method consists of separately analysing the heat transfer within each of these constituents and of imposing continuity of temperature and heat flux on their interfaces. Figure 1 shows a typical finite element mesh covering the whole furnace. Each separate object (e.g. A, B, C, ...) constitutes a *macro-element*. The analysis will make use of several sorts of macro-elements which are defined below.

A *radiative macro-element* is an enclosure bounded by one or more macro-elements of another type, where heat transfer between walls is essentially radiative (it is also possible to include convective transfer due to the motion of the ambient gas). Temperatures and heat fluxes are only evaluated on the walls of the enclosure. Since each wall of an enclosure may see the other walls, a radiative enclosure cannot be subdivided into smaller entities.

A *two-dimensional macro-element* is a liquid or solid component where heat transfer occurs by conduction (and possibly by convection). It is always allowed to partition a conductive (but not convective) macro-element into smaller entities without modifying the transfer properties of the system.

A *one-dimensional macro-element* is a specific entity designed for components which have a low thickness as compared to their other dimensions. Typically, the walls F of the enclosure G may be well described as a thin shell on which a relationship exists between the outgoing flux and the local temperature.

Parts of the boundary of a macro-element may either see the outer world, or be interfaced with another macro-element. The set of interfaces connecting macro-elements constitutes the *skeleton* of the global domain. In the following sections, we will show that the global heat transfer calculation consists of reducing it to an evaluation of nodal temperatures on the skeleton of the furnace. The cost of the calculation is essentially related to the number of nodes found on the skeleton.

We will now separately consider each type of macro-element while their assembly will be analysed in Section 6.

3. RADIATIVE ENCLOSURES

In this section, we shall focus on the modelling of radiative heat exchange, which plays a major role in Czochralski growth because natural emission in the infra-red part of the spectrum is important at the melting temperature of common semiconductors. We will follow the general theory of Siegel and Howell [19], although simplifications are required for the numerical simulation. Our main assumption is that radiation is only diffuse. This hypothesis is satisfactory even when specular reflection occurs, since true reflecting surfaces are generally non-smooth. Moreover, we shall consider that emission, absorption and reflection of radiating waves only occur at the surfaces of the bodies (and not within the bodies them-

selves). Further hypotheses will be introduced at a later stage.

3.1. Radiative exchanges in a fixed range of wavelengths

Let us first establish the integral equation governing radiative exchange in a given enclosure (delimiting a volume V) within a fixed range $\Lambda = [\lambda_1, \lambda_2]$ of wavelengths. We assume that all surfaces are opaque and all material properties are temperature and wavelength independent in this fixed range. In further subsections, we shall extend the model to more general situations, including the case of semi-transparent materials.

The radiation equation represents a balance between heat emission, absorption and reflection. Except at the absolute zero, all bodies emit energy in the form of electromagnetic waves. In the case of a black body (or a perfect absorber), natural emission obeys Planck's law, which has been determined on the basis of thermodynamic considerations. Let $e_{b\Lambda}(T)$ denote the spectral emissive power of the black body, i.e. the density of total power emitted by the body per unit wavelength at absolute temperature T and wavelength λ . Planck's law is written as follows:

$$e_{b\Lambda}(T) = \frac{2\pi C_1}{\lambda^5 (e^{C_2/\lambda T} - 1)} \quad (1)$$

where $C_1 = 0.595448 \times 10^8 \text{ W } \mu\text{m}^4 \text{ m}^{-2}$ and $C_2 = 14388 \mu\text{m K}$ are absolute constants. Curves of $e_{b\Lambda}(T)$ as a function of λ are given in Fig. 2 for various values of T .

The total power $q_{b\Lambda}(T)$ emitted by the black body per unit area over the range Λ of wavelengths is obtained by integration of equation (1) over this range; one obtains

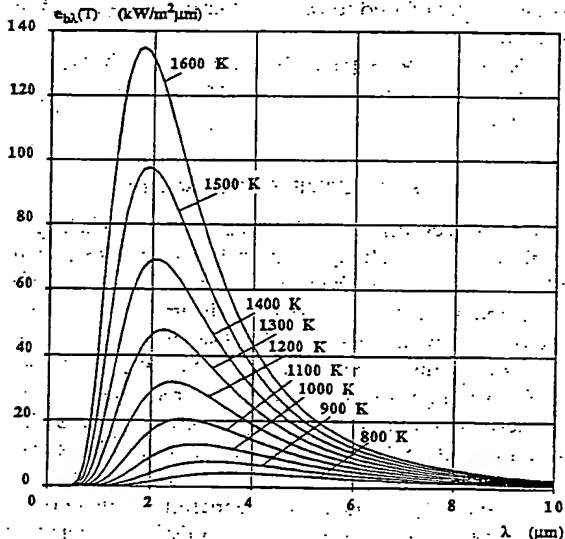


FIG. 2. Spectral emissive power of a black body for several temperatures.

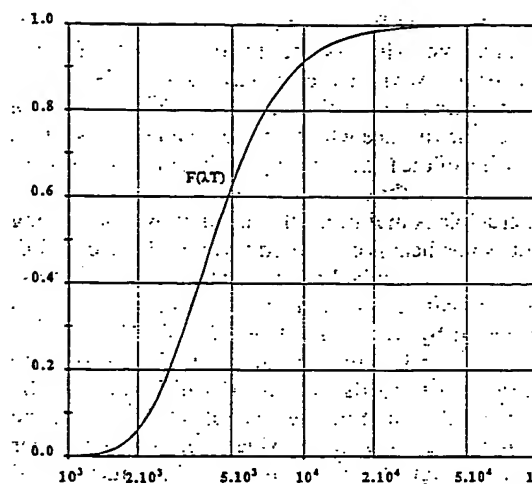


FIG. 3. Fractional black body emissive power in range 0 to λ_2 .

$$q_{b\Lambda}(T) = \int_{\lambda_1}^{\lambda_2} e_{b\Lambda}(T) d\lambda \quad (2)$$

where $\sigma = 5.6696 \times 10^{-8} \text{ W m}^{-2} \text{ K}^{-4}$ is Boltzmann's constant and γ_Λ is defined by the difference

$$\gamma_\Lambda(T) = F(\lambda_2 T) - F(\lambda_1 T) \quad (3)$$

with

$$F(\xi) = \int_0^{\xi} \frac{15C_2^4 d\eta}{\pi^4 \eta^5 (e^{C_2/\eta} - 1)} \quad (4)$$

The curve $F(\xi)$ is given in Fig. 3. It is clear that $\gamma_\Lambda(T)$ is the ratio between the powers emitted by the black body in the range Λ and in the whole spectrum $[0, \infty]$, respectively, and so lies between 0 and 1. Moreover, we may observe that γ_Λ depends little upon T as long as

$$0.2 \times 10^4 \mu\text{m K} \leq \lambda_1 T \leq \lambda_2 T \leq 10^4 \mu\text{m K} \quad (5)$$

In what follows, we shall assume that one of the following situations occurs: (i) (5) holds; (ii) Λ is the whole spectrum ($\gamma_\Lambda = 1$); (iii) the temperature T can be estimated everywhere on the enclosure. Thus, in all three cases, we assume that γ_Λ is a known function of the position on the surface of the enclosure.

Natural emission from a real body is lower than that from a black body. As we consider diffuse radiation and assume that material properties are temperature and frequency independent in the range Λ , the total power $q_{e\Lambda}$ emitted by the body per unit surface in this range is given by the expression

$$q_{e\Lambda}(x) = \varepsilon_\Lambda(x) q_{b\Lambda}(T(x)) \quad (6)$$

where $\varepsilon_\Lambda(x)$ is the surface emissivity at the generic point x on the enclosure and takes values in the range $[0, 1]$.

Any element of area is also permanently bom-

barded by waves emitted (or reflected) from other points on the same enclosure. The incident heat flux $q_{i\Lambda}(x)$ can either penetrate the body or be reflected. Since we assume the surfaces to be opaque in the range Λ , the non-reflected waves are totally absorbed and transformed into internal energy in the body. Kirchhoff's law (which is a consequence of thermodynamic equilibrium in isothermal enclosures) states that the absorptivity of any surface, i.e. the ratio between the absorbed and incident heat fluxes, must exactly equal the surface emissivity. Hence, the absorbed and reflected heat fluxes in the range Λ , $q_{a\Lambda}(x)$ and $q_{r\Lambda}(x)$, are given respectively by

$$q_{a\Lambda}(x) = \varepsilon_\Lambda(x) q_{i\Lambda}(x) \quad (7)$$

and

$$q_{r\Lambda}(x) = (1 - \varepsilon_\Lambda(x)) q_{i\Lambda}(x). \quad (8)$$

As the total outgoing heat flux (or *radiosity*) $q_{o\Lambda}(x)$ is the sum of the emitted and reflected fluxes at x in the range Λ , we also have

$$q_{o\Lambda}(x) = q_{a\Lambda}(x) + q_{r\Lambda}(x) = \varepsilon_\Lambda(x) \gamma_\Lambda(x) \sigma T^4(x) + (1 - \varepsilon_\Lambda(x)) q_{i\Lambda}(x). \quad (9)$$

On the other hand, the total incident heat flux $q_{i\Lambda}(x)$ in the range Λ is the sum of the contributions of the outgoing fluxes $q_{o\Lambda}(x^*)$ from all other points on the enclosure. Let dS and dS^* be infinitesimal areas at points x and x^* . The fraction of the incident flux on dS which leaves dS^* is calculated by the product

$$dq_{i\Lambda}(x) = K(x, x^*) q_{o\Lambda}(x^*) dS^* \quad (10)$$

where $K(x, x^*)$ is the surface view factor between x and x^* . Lambert's cosine law for diffuse radiation states that, whenever dS and dS^* see each other, $K(x, x^*)$ is given by the formula

$$K(x, x^*) = - \frac{[(x^* - x) \cdot n][[(x^* - x) \cdot n^*]]}{\pi[(x^* - x) \cdot (x^* - x)]^2} \quad (11)$$

where n and n^* are the unit normals to dS and dS^* (Fig. 4). On the other hand, when dS and dS^* do not see each other, $K(x, x^*)$ vanishes

$$K(x, x^*) = 0. \quad (12)$$

From the knowledge of $K(x, x^*)$, it is easy to integrate equation (10) over the surface ∂V of the enclosure

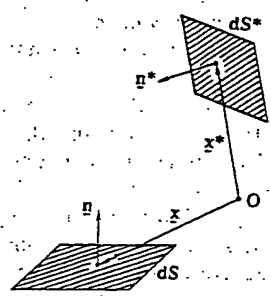


FIG. 4. Surface view factors between infinitesimal areas.

$$q_{i\Lambda}(x) = \int_{x^* \in \partial V} K(x, x^*) q_{o\Lambda}(x^*) dS^*. \quad (13)$$

Let $q_\Lambda(x)$ represent the net heat flux at x in the range Λ , assumed to be positive when the corresponding energy enters the enclosure. Clearly, $q_\Lambda(x)$ is the difference between the outgoing and incident heat fluxes at x

$$q_\Lambda(x) = q_{o\Lambda}(x) - q_{i\Lambda}(x). \quad (14)$$

Calculating $q_{i\Lambda}(x)$ and $q_{o\Lambda}(x)$ from equations (9) and (14) yields

$$\begin{cases} q_{i\Lambda}(x) = \gamma_\Lambda(x) \sigma T^4(x) - \frac{1}{\varepsilon_\Lambda(x)} q_\Lambda(x) \\ q_{o\Lambda}(x) = \gamma_\Lambda(x) \sigma T^4(x) - \frac{1 - \varepsilon_\Lambda(x)}{\varepsilon_\Lambda(x)} q_\Lambda(x). \end{cases} \quad (15)$$

Thus, introducing equations (15) in equation (13), one finds that the surface temperatures $T(x)$ and heat fluxes $q_\Lambda(x)$ on ∂V are related by the integral relationship

$$\begin{aligned} \frac{q_\Lambda(x)}{\varepsilon_\Lambda(x)} &= \int_{x^* \in \partial V} K(x, x^*) \frac{1 - \varepsilon_\Lambda(x^*)}{\varepsilon_\Lambda(x^*)} q_\Lambda(x^*) dS^* \\ &= \gamma_\Lambda(x) \sigma T^4(x) - \int_{x^* \in \partial V} K(x, x^*) \gamma_\Lambda(x^*) \sigma T^4(x^*) dS^*. \end{aligned} \quad (16)$$

In order to obtain a manageable system of equations, equation (16) must first be transformed for taking into account the axisymmetry of the furnace. To this end, let r , θ and z denote the cylindrical coordinates of x and $p(\partial V)$ stand for the intersection of the enclosure surface ∂V and the mid-halfplane $\theta = 0$ (a schematic enclosure is represented in Fig. 5). Further, let s be the curvilinear abscissa on $p(\partial V)$. For any x on $p(\partial V)$, we rewrite equation (16) in the form

$$\begin{aligned} \frac{q_\Lambda(x)}{\varepsilon_\Lambda(x)} &= \int_{x^* \in p(\partial V)} r' K_c(x, x^*) \frac{1 - \varepsilon_\Lambda(x^*)}{\varepsilon_\Lambda(x^*)} q_\Lambda(x^*) ds' \\ &= \gamma_\Lambda(x) \sigma T^4(x) - \int_{x^* \in p(\partial V)} r' K_c(x, x^*) \gamma_\Lambda(x^*) \sigma T^4(x^*) ds' \end{aligned} \quad (17)$$

where the axisymmetric view factor $K_c(x, x^*)$ is defined by the integral

$$K_c(x, x^*) = 2 \int_0^\pi K(x, x^*) d\theta^* \quad (18)$$

with

$$\begin{cases} x = (r, 0, z) \in p(\partial V) \\ x' = (r', 0, z') \in p(\partial V) \\ x^* = (r' \cos \theta^*, r' \sin \theta^*, z') \in \partial V. \end{cases} \quad (19)$$

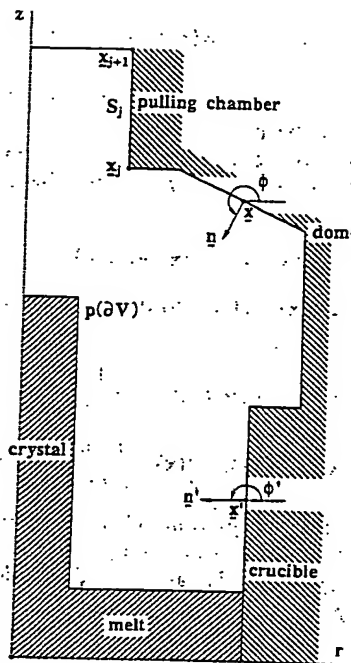


FIG. 5. Schematic enclosure section for an axisymmetric furnace ($m = 10$).

Note that, throughout this section, we always represent vectors (including position vectors) in Cartesian components, as in equations (19). The calculation of $K_c(x, x')$ from equations (18), (11) and (12) is very complex, since the viewed and hidden parts of the enclosure must be taken into account. The complete procedure is described in the next subsection.

3.2. Axisymmetric calculation of the shape factor in the enclosure

We will assume that the enclosure boundary ∂V is generated by the rotation around the z -axis of m , rectilinear sides S_j forming the enclosure section $p(\partial V)$ (Fig. 5). Each side is delimited by the edges x_j and x_{j+1} , with

$$x_j = (r_j, 0, z_j). \quad (20)$$

For any pair (x, x') belonging to the section of the enclosure, we need to calculate the axisymmetric view factor $K_c(x, x')$, as defined by equations (18) and (19). For convenience, we shall assume that, for a fixed pair (x, x') , x^* is a current point of azimuthal coordinate θ^* related to x' by equations (19). Moreover, n and n' will denote the unit normals to the enclosure at points x and x' , with

$$\begin{cases} n = (\cos \phi, 0, \sin \phi) \\ n' = (\cos \phi', 0, \sin \phi') \end{cases} \quad (21)$$

The unit normal n^* at the current point x^* is thus given (in Cartesian components) by

$$n^* = (\cos \phi' \cos \theta^*, \cos \phi' \sin \theta^*, \sin \phi'). \quad (22)$$

Whenever x and x^* see each other, the view factor $K(x, x^*)$ does not vanish and is given by equation (11). Introducing equations (19), (21) and (22) in equation (11), we can express the dependence of $K(x, x^*)$ with respect to θ^* . We thus rewrite $K(x, x^*)$ in the form of a function $\hat{K}(\theta^*)$

$$K(x, x^*) = \hat{K}(\theta^*) = \frac{(a' + b' \cos \theta^*)(a'' + b'' \cos \theta^*)}{(a + b \cos \theta^*)^2} \quad (23)$$

where a, b, a', b', a'' and b'' only depend on r, z, r', z', ϕ and ϕ' (which are fixed) but not on θ^* . These coefficients will not be developed in detail. Integrating equation (23) with respect to θ^* yields a primitive function $I(\theta)$ of $\hat{K}(\theta^*)$

$$\begin{aligned} I(\theta) &= \int_0^\theta \hat{K}(\theta^*) d\theta^* \\ &= A\theta + B \tan^{-1} \left(\sqrt{\left(\frac{a-b}{a+b} \right) \tan \theta/2} \right) \\ &\quad + C \frac{\sin \theta}{a+b \cos \theta} \end{aligned} \quad (24)$$

where coefficients A, B and C are suitable functions of $a, b; a', b', a''$ and b'' [12].

Consider now the integral (18). Let Θ denote the range of values of θ^* for which $K(x, x^*)$ does not vanish. In order to calculate the axisymmetric view factor $K_c(x, x')$ we only need to characterize Θ as a set of l intervals $[\theta_{mi}, \theta_{Mi}]$

$$\Theta = \bigcup_{i=1}^l [\theta_{mi}, \theta_{Mi}], \quad 0 \leq \theta_{mi} < \theta_{Mi} \leq \pi \quad (25)$$

since equations (18), (23) and (24) then provide the expected result

$$K_c(x, x') = 2 \sum_{i=1}^l (I(\theta_{Mi}) - I(\theta_{mi})). \quad (26)$$

It is clear that Θ depends on the viewed and hidden parts of the enclosure. We will therefore analyse this last problem in detail.

Generally, we thus wish to determine whether any given line x^*x is intersected or not by the enclosure boundary. To this end, we define the circular projection $p(y)$ of any point y of the line x^*x as being the point on the mid-halfplane $\theta = 0$ having the same radial and axial coordinates as y . It is easy to prove that any projected line $p(x^*x)$, i.e. the set of circular projections of the points forming the line x^*x , is a segment of a hyperbola (Figs. 6 and 7). We may consider a straight line which is rigidly linked to the axis of symmetry and which is initially identical to x^*x ; letting this segment rotate around the axis of symmetry will generate a one sheet hyperboloid which intersects the mid-halfplane $\theta = 0$ through a hyperbola passing through x and $x' = p(x^*)$. In particular,

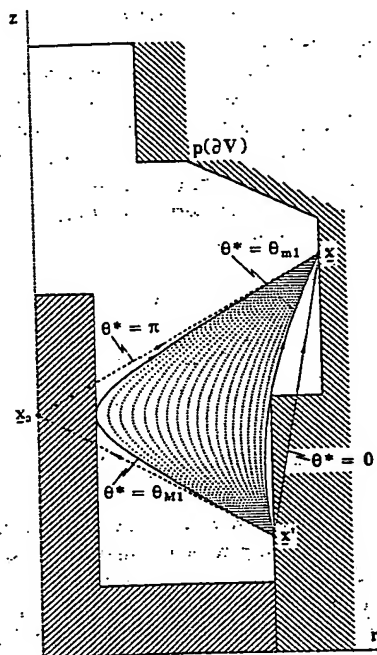


FIG. 6. Projected lines passing through x' and x for a simply connected enclosure section ($l=1$). The family is indexed by the azimuthal coordinate θ^* of x^* , with $x' = p(x^*)$.

the line $\overline{x'x}$ obviously forms its own projection. Moreover, the line $\overline{\hat{x}'x}$, where \hat{x}' is the symmetric of x' with respect to the z -axis, as defined (in Cartesian components) by

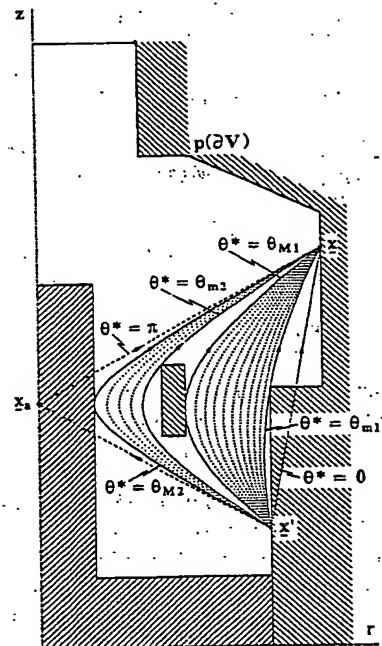


FIG. 7. Same legend as in Fig. 6 for a multi-connected enclosure section ($l=2$).

$$\hat{x}' = (-r', 0, z') \quad (27)$$

is projected on the pair of segments $\overline{x'x_a}$ and $\overline{x_a x}, x_a$ being the intersection of $\hat{x}'x$ with the z -axis.

$$x_a = \left(0, 0, \frac{r'z + rz'}{r' + r} \right) \quad (28)$$

Hence, letting θ^* (and thus x^*) vary in equations (19), the set of projected lines $p(x^*x)$ will form a bundle of hyperbolas passing through x and x' and contained in the triangle (x, x', x_a) . The angle θ^* varies between 0 (if $x^* = x'$) and π (if $x^* = \hat{x}'$) and will be considered as the parameter of this set.

Besides the fact that they provide a tool for understanding radiative exchange in axisymmetric furnaces, the importance of projected lines lies in the following observation: for any line x^*x , interception occurs if, and only if, the projected line $p(x^*x)$ crosses the enclosure section $p(\partial V)$. Equivalently, a line x^*x is not intercepted if, and only if, its projection $p(x^*x)$ does not cross any side S_j of $p(\partial V)$. This property will allow us to calculate the axisymmetric view factor $K_c(x, x')$. For any side S_j of $p(\partial V)$ (Fig. 8), we define the interval $[\theta_{m_j}, \theta_{M_j}]$ as the range of values of the azimuthal coordinate θ^* of x^* such that the projected line $p(x^*x)$ is intercepted by S_j .

$$\theta^* \in [\theta_{m_j}, \theta_{M_j}] \Rightarrow K(x, x^*) = 0. \quad (29)$$

Note that these intervals may be empty and may also overlap. The range Θ of values for which $K(x, x^*)$ does not vanish is thus given by

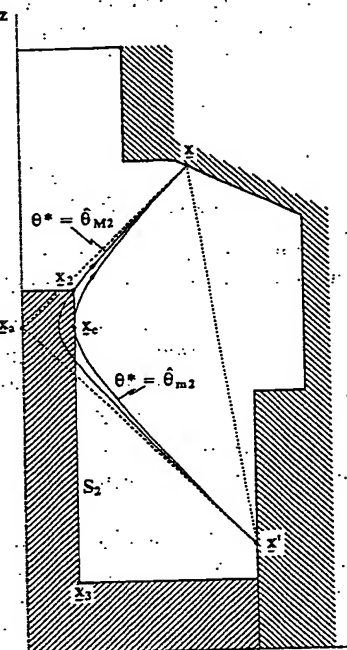


FIG. 8. Interception of a family of projected lines by a side (S_2) of the enclosure section.

$$\Theta = [0, \pi] \cup \bigcup_{j=1}^m [\theta_{mj}, \theta_{Mj}]. \quad (30)$$

Since knowledge of Θ provides $K_c(x, x')$ from equations (26) and (25), it is clear that our final problem lies in determining the intervals $[\theta_{mj}, \theta_{Mj}]$. These can easily be calculated by applying the theorem which follows.

Theorem. Let S_j be any side of the enclosure section $p(\partial V)$, with extremities x_j and x_{j+1} given by equation (20). Let also x be a fixed point on $p(\partial V)$ and x^* be, on the enclosure ∂V , a point of unknown azimuthal coordinate θ^* and fixed circular projection x' (as given by equations (19)). Two cases are considered (Fig. 8):

(i) if the projected line $p(\overline{x^*x})$ passes through x_j , then θ^* can be obtained by solving the equation

$$\cos \theta^* = \frac{r_j^2(z' - z)^2 - r'^2(z_j - z)^2 - r^2(z' - z_j)^2}{2r'(z_j - z)(z' - z_j)}; \quad (31)$$

(ii) if $p(\overline{x^*x})$ is tangent to S_j , then θ^* can be obtained by solving the system

$$\begin{cases} \theta^* = \theta + \theta' \\ \cos \theta = \frac{z(r_{j+1} - r_j) + (r_j z_{j+1} - r_{j+1} z_j)}{r(z_{j+1} - z_j)} \\ \cos \theta' = \frac{z'(r_{j+1} - r_j) + (r_j z_{j+1} - r_{j+1} z_j)}{r'(z_{j+1} - z_j)} \end{cases} \quad (32)$$

When they occur, indeterminacies must be removed by application of L'Hospital's rule. In both cases, the searched projected line exists if, and only if, equations (31) or (32) have a real solution. Moreover, in the second case, the coordinates of the contact point x_c , when it exists, are given by the formulae

$$\begin{cases} r_c = \frac{rr' \sin(\theta + \theta')}{r \sin \theta + r' \sin \theta'} \\ z_c = \frac{zr' \sin \theta' + z'r \sin \theta}{r \sin \theta + r' \sin \theta'} \end{cases} \quad (33)$$

The proof of this theorem is solely based on geometrical considerations and will be omitted.

Let us now return to the calculation of the intervals $[\theta_{mj}, \theta_{Mj}]$. The previous discussion shows that θ_{mj} and θ_{Mj} must be chosen as the lowest and highest value of θ^* , respectively, between the following:

(i) $\theta^* = 0$ or (and) $\theta^* = \pi$, if S_j intersects one or both of the degenerate projected lines $\overline{x^*x}$ and $\overline{x^*x_{j+1}}$;

(ii) the values of θ^* obtained by applying the previous theorem (first case) to x_j or (and) x_{j+1} , if one or both of these are located inside the triangle (x, x_c, x') ;

(iii) the value of θ^* obtained by applying the previous theorem (second case), if the contact point x_c is located between x_j and x_{j+1} , and inside the triangle (x, x_c, x') .

3.3. Discretization of the radiative integral equation

Any radiating enclosure of the furnace is discretized by means of a set of n one-dimensional finite elements. The approximation of temperatures and heat fluxes is everywhere continuous on the enclosure section $p(\partial V)$, except at its edges (where analytical heat fluxes are normally discontinuous). Using quadratic shape functions, we write in equations (17) (for wavelengths in the range Λ)

$$\begin{cases} q_\Lambda(x) = \sum_i q_{\Lambda i} \psi_i(x) \\ T^4(x) = \sum_i T_i^4 \psi_i(x) \end{cases} \quad (34)$$

We thus approximate

$$\left(\sum_i T_i \psi_i(x) \right)^4 \text{ by } \sum_i T_i^4 \psi_i(x).$$

Numerical experiments have shown the validity of such an approximation which considerably simplifies our calculations.

We discretize the integral equation (17) on the basis of a Galerkin formulation. This method has been preferred to a procedure of nodal collocation because, in the latter case, important numerical problems arise from the calculation of the axisymmetric view factor $K_c(x, x')$ at the edges of $p(\partial V)$. Thus, discrete equations are obtained by multiplying both sides of equation (17) by $(r\psi_i(x) ds)$ and integrating the result over $p(\partial V)$:

$$\begin{aligned} & \sum_j \left[\int_{p(\partial V)} \frac{1}{\varepsilon_\Lambda(x)} \psi_i(x) \psi_j(x) ds \right. \\ & \quad \left. - \int_{p(\partial V)} r\psi_i(x) \int_{p(\partial V)} r' K_c(x, x') \frac{1 - \varepsilon_\Lambda(x')}{\varepsilon_\Lambda(x')} \right. \\ & \quad \left. \times \psi_j(x') ds' ds \right] q_{\Lambda j} \\ & = \sum_j \left[\int_{p(\partial V)} r\gamma_\Lambda(x) \psi_i(x) \psi_j(x) ds \right. \\ & \quad \left. - \int_{p(\partial V)} r\psi_i(x) \int_{p(\partial V)} r' K_c(x, x') \gamma_\Lambda(x') \right. \\ & \quad \left. \times \psi_j(x') ds' ds \right] \sigma T_i^4. \end{aligned} \quad (35)$$

After suitable matrix operations, the system (35) may then be written in the form

$$q_\Lambda = \underline{F}_\Lambda T^4 \quad (36)$$

where q_Λ and T^4 respectively denote the column vectors of nodal heat fluxes (in the range Λ) and fourth power of temperatures, and \underline{F}_Λ is now a known matrix. It is clear that either Λ extends over the whole spectrum $[0, \infty]$, and $q_\Lambda(x)$ is the total heat flux $q(x)$ entering the enclosure, or several ranges of wavelengths $\Lambda_1, \Lambda_2, \dots$ must be considered. In the former case, dropping the index Λ in equation (36), we write

$$q = FT^4. \quad (37)$$

In the latter case, we have

$$\begin{aligned} q &= q_{A_1} + q_{A_2} + \dots \\ &= (F_{A_1} + F_{A_2} + \dots)T^4 \end{aligned} \quad (38)$$

and thus the total heat flux depends on the fourth power of temperature as before. Equation (37) is the general discretized relationship governing radiative exchange in an enclosure. The case of semi-transparent materials also reduces to this form and will be investigated in the next subsection.

Numerical integration of equation (35) with respect to ds is performed with a three node Gaussian quadrature on every element, while 20 nodes are used for the integration with respect to ds' . This choice is justified by the steep variations of $K_c(x, x')$ observed in the vicinity of the edges of $p(\partial V)$. However, even with such an accurate method, poor results have been obtained in some circumstances. It is possible to check the accuracy of the integration with the help of the identity

$$\int_{p(\partial V)} r' K_c(x, x') ds' = 1. \quad (39)$$

In the worst cases, the left-hand side was equal to 0.3–0.2. We have found that the origin of this problem lies in the fact that the axisymmetric view factor is not a regular function, whereas this is required for applying Gaussian quadrature. We have therefore improved the algorithm in the following way: as equation (35) is integrated with respect to both ds and ds' , the integration with respect to ds' must be performed for any given integration node x (recall that three such nodes are located on any element). For any fixed x , we divide the enclosure section $p(\partial V)$ at any point $x_{(1)}, x_{(2)}, \dots$ where $K_c(x, x')$ is a discontinuous function of x' , or has a discontinuous derivative with an infinite slope on one or both sides of the discontinuity. For any element where such a division point is located, a 20 node Gaussian integration (with respect to ds') is then performed separately on both parts of the element.

It is possible to prove that $K_c(x, x')$ is not regular in x' (in the previous sense), whenever one of the degenerate lines $x'x$ ($\theta^* = 0$) or $x'x_* \cup x_*x$ ($\theta^* = \pi$) passes through one of the edges of the enclosure section. These cases can be easily detected (Fig. 9). On this basis, the improved algorithm can provide accurate results as long as the identity (39) is used to check the validity of the mesh of the enclosure: generally, when two elements are adjacent to a re-entrant edge of $p(\partial V)$, their respective sizes must be of the same order of magnitude.

We conclude this subsection by noting that Galerkin's method is globally conservative, which means that the total heat flux balance would vanish on the enclosure if integrations were performed exactly. As a matter of fact, the identity

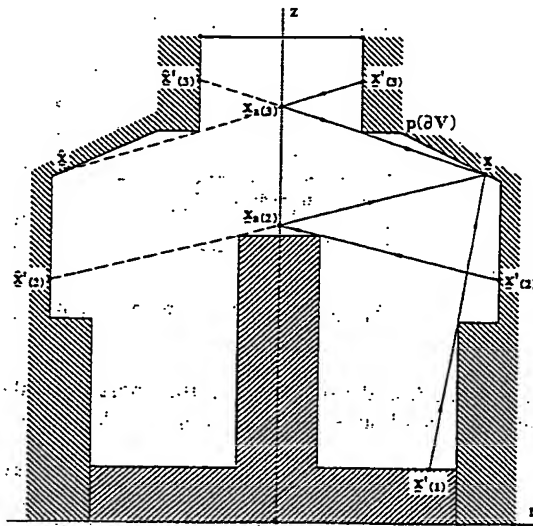


FIG. 9. Degenerate projected lines passing through one of the edges of the enclosure section $p(\partial V)$.

$$\sum_i \psi_i(x) = 1 \quad (40)$$

can be introduced in equation (35) through the sum of the latter equations (which are indexed by i). Reversing the order of integrations, taking into account the symmetry of the kernel $K_c(x, x')$, and using the identity (39), one can then obtain

$$\sum_j \left[\int_{p(\partial V)} r' \psi_j(x') ds' \right] q_{A_j} = 0 \quad (41)$$

or equivalently, using equations (34)

$$\int_{p(\partial V)} q_{A_j}(x^*) ds^* = 0. \quad (42)$$

3.4. Semi-transparent materials

The boric oxide layer used in the Czochralski growth of gallium arsenide for avoiding arsenic evaporation is not opaque and thus one of the hypotheses specified in the first subsection does not hold. In a semi-transparent medium, absorption does not take place solely at the surface of the body. Energy is partly transmitted through the body, and also absorbed and emitted within the body itself.

Let us consider a monochromatic ray of wavelength λ , with an initial intensity I_1^0 , which crosses (without reflection) a material of thickness h . It is attenuated by absorption and dispersion. Neglecting the latter, Bouguer's law gives a relationship between the outgoing intensity I_2^h and the absorption coefficient a_λ :

$$I_2^h = I_1^0 \exp(-a_\lambda h). \quad (43)$$

The penetration depth L_λ is defined as

$$L_\lambda = \frac{1}{a_\lambda}. \quad (44)$$

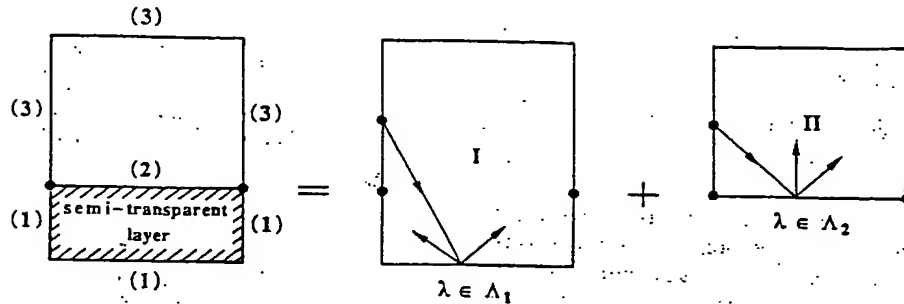


FIG. 10. Application of the band-energy method for calculating heat exchange in a semi-transparent material.

Comparing this depth with the thickness h of the material, one obtains the spectral optical thickness τ_1

$$\tau_1 = \frac{L_1}{h} \quad (45)$$

When τ_1 is large compared to one, the material is transparent for the wavelength λ ; when τ_1 is small compared to one, the material is opaque for the wavelength λ . Our model assumes that the ranges of wavelengths for which τ_1 is of the same order as one are negligible; using the band-energy method, we thus consider that the boric oxide layer is transparent for some ranges of wavelengths ($\tau_1 > 1$) and opaque for others ($\tau_1 < 1$).

On this basis, it is easy to calculate radiative heat exchange in a semi-transparent medium. Let us consider a simplified example, represented in Fig. 10, where we have a semi-transparent layer. We define two different enclosures, where radiative exchanges take place with different wavelengths. Enclosure I corresponds to waves (in the range Λ_1) for which the layer is transparent, while enclosure II corresponds to waves (in the range Λ_2) for which it is opaque. Within each enclosure, radiative exchange is governed by the integral equation (17), which is approximated by equation (36). We separate the boundaries of the domain into three groups, denoted by (1), (2), (3) (see Fig. 10): boundaries (3) are common to both enclosures, while boundaries (1) and (2) belong to enclosures I and II only. The total radiating heat flux $q(\mathbf{x})$ is thus given by

$$\begin{cases} q(\mathbf{x}) = q_{\Lambda_1}(\mathbf{x}) & \text{on (1)} \\ q(\mathbf{x}) = q_{\Lambda_2}(\mathbf{x}) & \text{on (2)} \\ q(\mathbf{x}) = q_{\Lambda_1}(\mathbf{x}) + q_{\Lambda_2}(\mathbf{x}) & \text{on (3)} \end{cases} \quad (46)$$

It is therefore possible to obtain a general law of the form of equation (37) over the whole boundary by superposing (as in equation (38)) the contributions of each enclosure. The resulting enclosure may be considered as a single radiative macro-element.

4. TREATMENT OF TWO- AND ONE-DIMENSIONAL MACRO-ELEMENTS

In this section, we wish to study macro-elements where heat is transferred by conduction, such as the

heater and the crucible, with the exception of the melt and the crystal which will be considered separately in Section 5. In such macro-elements, the temperature field is governed by the equation

$$\nabla \cdot [k(\mathbf{x}) \nabla T(\mathbf{x})] + r(\mathbf{x}) = 0 \quad (47)$$

where k is the thermal conductivity which may depend upon the position \mathbf{x} and r is a heat source per unit volume which will in general depend upon \mathbf{x} . For simplicity, we assume that k is temperature independent in order to preserve the linearity of the system. We will first discuss the case of two-dimensional macro-elements:

The macro-element is covered by a mesh of finite elements which in the present paper are six-node triangles or nine-node quadrilaterals. The approximate temperature field is represented by the sum

$$\tilde{T} = \sum_i T_i \phi_i \quad (48)$$

where the T_i 's are nodal temperatures forming a vector \mathbf{T} and the ϕ_i 's are the corresponding global shape functions. Let Ω be the axisymmetric domain corresponding to the macro-element; applying Galerkin's method for discretizing equation (47), one obtains

$$\int_{\Omega} \phi_i [\nabla \cdot (k \nabla T) + r] d\Omega = 0 \quad (49)$$

or, with an integration by parts

$$\int_{\Omega} k (\nabla \phi_i \cdot \nabla T) d\Omega = \int_{\Omega} \phi_i r d\Omega - \int_{\Sigma} \phi_i q d\Sigma \quad (50)$$

where Σ is the boundary of Ω and q is the outgoing heat flux, as given by

$$q = -k \nabla T \cdot \mathbf{n} \quad (51)$$

\mathbf{n} being the outer normal on Σ . The boundary Σ is the union of two parts, Σ^+ and Σ^0 (Fig. 11); Σ^+ belongs to the skeleton of the furnace defined in Section 2, while Σ^0 is the part of the outer boundary where the temperature is fixed or is related to the heat flux density q by a law such as

$$q = h(T - T_0) \quad (52)$$

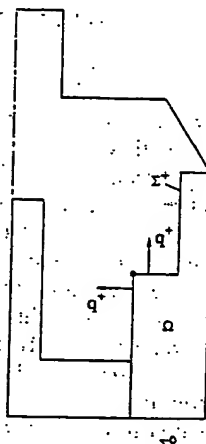


FIG. 11. Boundary partition for the calculation of heat transfer in a conductive macro-element.

where h is a convection coefficient ($\text{W m}^{-2} \text{K}^{-1}$) and T_0 is the coolant temperature.

Let \mathbf{T}^+ denote the vector of nodal temperatures on Σ^+ and let \mathbf{T}^* denote the vector of all other nodal temperatures associated with the macro-element; we write

$$\mathbf{T} = [\mathbf{T}^*, \mathbf{T}^+]. \quad (53)$$

It is then easy to rewrite equation (50) in the following form:

$$\underline{\mathbf{M}}^* \mathbf{T}^* + \underline{\mathbf{M}}^+ \mathbf{T}^+ = \mathbf{E}^*(W) - \mathbf{Q}^+ \quad (54)$$

where the following symbols have been introduced:

$$\begin{aligned} \underline{\mathbf{M}}^* &= \left\{ \int_{\Omega} k(\nabla \phi_i \cdot \nabla \phi_j) d\Omega + \int_{\Sigma^0} h(\phi_i, \phi_j) d\Sigma \right\} \\ \underline{\mathbf{M}}^+ &= \left\{ \int_{\Omega} k(\nabla \phi_i \cdot \nabla \phi_j) d\Omega \right\} \\ \underline{\mathbf{N}} &= \left\{ \int_{\Omega} k(\nabla \phi_i \cdot \nabla \phi_j) d\Omega \right\} \\ \mathbf{E}^*(W) &= \left\{ \int_{\Omega} \phi_i r d\Omega + \int_{\Sigma^0} \phi_i h T_0 d\Sigma \right\} \\ \mathbf{E}^+(W) &= \left\{ \int_{\Omega} \phi_i r d\Omega \right\} \\ \mathbf{Q}^+ &= \left\{ \int_{\Sigma^+} \phi_i q d\Sigma \right\}. \quad (55) \end{aligned}$$

The superscripts * and + refer to the partition of nodal temperatures, as defined in equation (53). The symbol W in equations (54) represents the total power input in the macro-element which, at this stage, may be unknown.

In order to link at a later stage the two-dimensional macro-element with the adjacent radiative enclosures

or with any other macro-element, we need a representation of the heat flux density q along Σ^+ . The latter is assumed to be

$$q = \sum q_i \phi_i \quad (56)$$

in terms of nodal flux densities and shape functions. The number of nodal flux densities along Σ^+ may be larger than the number of nodal temperatures. Indeed, if Σ^+ has corners, we will associate two nodal heat flux densities at these corners, one for each adjacent section of the skeleton (Fig. 12); we will show in Section 6 how to handle such multiple values in the global calculation on the skeleton. Let \mathbf{q}^+ denote the vector of nodal heat flux densities on Σ^+ ; its dimension may thus be larger than that of \mathbf{T}^+ . Combining equation (56) and the sixth equation (55), one obtains a relationship of the form

$$\mathbf{Q}^+ = \underline{\mathbf{B}}^+ \mathbf{q}^+ \quad (57)$$

which is introduced in equation (54).

At this stage, it is possible to perform a *static condensation* of the macro-element or, in other words, to eliminate \mathbf{T}^* from the system (54). Formally, if one defines the matrix

$$\underline{\mathbf{A}}^+ = \underline{\mathbf{M}}^+ - \underline{\mathbf{N}}^T \underline{\mathbf{M}}^{*-1} \underline{\mathbf{N}} \quad (58)$$

and the vector

$$\mathbf{C}^+(W) = \mathbf{E}^+(W) - \underline{\mathbf{N}}^T \underline{\mathbf{M}}^{*-1} \mathbf{E}^*(W) \quad (59)$$

one obtains the system

$$\underline{\mathbf{A}}^+ \mathbf{T}^+ + \underline{\mathbf{B}}^+ \mathbf{q}^+ = \mathbf{C}^+(W) \quad (60)$$

Such a static condensation is easy to perform when the frontal elimination method is used. We have thus shown that it is possible to reduce a heat conducting macro-element to a linear relationship between the nodal temperatures and the nodal heat fluxes on that part of its boundary which belongs to the skeleton. The system will be closed when the various macro-elements are connected by means of the radiative enclosures.

We have seen in Section 2 that, for some parts of the furnace, it is interesting to use one-dimensional

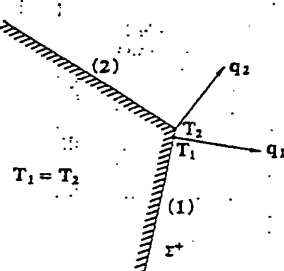


FIG. 12. Nodal flux densities and temperatures at the corners of the boundary.

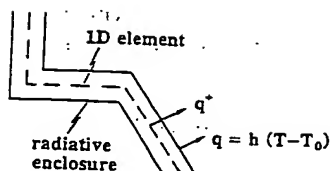


FIG. 13. Example of a one-dimensional macro-element on the upper dome of a Czochralski furnace.

macro-elements. An example is given in Fig. 13: the upper radiative enclosure is adjacent to a thin shell (representing the dome) which is part of the skeleton. The loss of heat along the outer side of such a macro-element is again given by a relationship of the type of equation (52); since the macro-element does not accumulate heat, we may thus write

$$q^+ + h(T^+ - T_0) = 0 \quad (61)$$

where q^+ denotes the heat flux density towards the skeleton. Using Galerkin's method with a representation similar to equations (48) and (56), it is easy to obtain an equation of the form

$$A^+ T^+ + B^+ q^+ = 0 \quad (62)$$

for the one-dimensional macro-element.

Let us close this section by mentioning a particular use of one-dimensional macro-elements which is found useful for dividing a radiative enclosure in two entities with negligible interaction between them; an example is given in Fig. 14. Two adjacent one-dimensional macro-elements are then used, with the constraint that nodal temperatures at adjacent nodes are identical while the sum of the corresponding nodal heat flux densities vanishes.

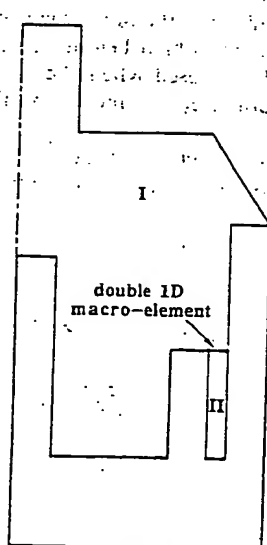


FIG. 14. Use of a twin one-dimensional macro-element for subdividing a radiative enclosure in two parts.

5. THE CRYSTAL-MELT MACRO-ELEMENT

In this section, we wish to study the domain formed by the crystal and the melt. It will be found important to associate these two components within a single macro-element, because they are separated by the liquid-solid interface which is *a priori* unknown. The interface originates at the point of intersection of the solid, liquid and gas (or oxide in LEC growth) domains, or tri-junction, where the temperature must be equal to the melting temperature of the crystal.

Locating the interface is more difficult with the Czochralski growth (see, e.g. ref. [34]) than with the Bridgman process (see, e.g. ref. [35]). In the first case, an appropriate combination of pulling rate and power input must be calculated in order to grow a crystal with a constant predefined radius; we will show that the optimal technique consists of imposing the crystal diameter and the growth rate, and of getting the heater input power as a result. In the second case, the interface is simply defined by the melting isotherm, and the tri-junction is thus an additional degree of freedom; this means that the pulling rate and the input power may be imposed, while the interface location results from the calculation.

5.1. Basic equations

A cross-section of a schematic crystal-melt macro-element is shown in Fig. 15. The axisymmetric domain Ω is the union of a solid region Ω_s and a liquid region Ω_L , separated by an interface Γ . Our mathematical model relies on a set of hypotheses which we repeat for the sake of clarity:

- (i) the quasi-steady state hypothesis allows us to neglect the partial time derivatives in the governing equations;
- (ii) the length and the radius of the crystal are imposed but the location of the interface is unknown;
- (iii) the shape of the free surface of the melt is imposed at the outset of the global calculation; in particular, the shape of the meniscus linking the crystal to the surface of the melt is calculated separately (see Section 5.4);
- (iv) additionally, we will neglect the change of density from the liquid to the solid domain.

When the motion of the melt is taken into account, heat transfer in the liquid domain is governed by the following equation:

$$\rho c v \cdot \nabla T - \nabla \cdot (k_L \nabla T) = 0 \quad (63)$$

where v is the velocity field in the melt, ρ the density, c the heat capacity and k_L the thermal conductivity. In the solid domain, we have

$$\nabla \cdot (k_s \nabla T) = 0 \quad (64)$$

where k_s is the thermal conductivity in the crystal. In view of the low growth rate of the crystal, vertical heat convection can be neglected by comparison with the diffusive term.

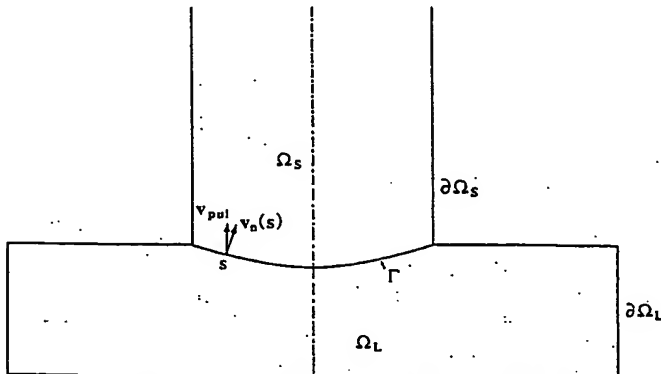


FIG. 15. Cross-section of the crystal-melt macro-element.

In order to evaluate the release of latent heat of fusion along the interface Γ , let us denote by $v_n(s)$ the normal growth velocity of the crystal along the interface as a function of an arc length s , with respect to a frame attached to the seed; thus, v_n is positive during growth. The amount of solidification per unit time and area along Γ is the product ρv_n , and the corresponding release of heat is given by

$$W_\Gamma(s) = \rho \Delta H_f v_n(s) \quad (65)$$

where ΔH_f is the specific latent heat of fusion of the crystal. Under quasi-steady assumption, the normal velocity v_n is related to the pulling rate v_{pul} of the crystal by the relationship

$$v_n(s) = -v_{\text{pul}} n_s \cdot e_z \quad (66)$$

where e_z is a unit vector pointing upwards and n_s is the outer unit normal to Ω_s along Γ .

Denoting by q_L and q_s the local outgoing heat flux densities along Γ , we require that the energy balance be preserved along the interface and thus

$$W_\Gamma(s) + q_L(s) + q_s(s) = 0. \quad (67)$$

If one neglects supercooling, the location of the interface itself is found through its identification with the melting point isotherm, i.e.

$$T(s) = T_m \text{ along } \Gamma. \quad (68)$$

5.2. Spatial discretization

Since the location of Γ is a priori unknown, the discretized form of the basic equations must be established on a deformable finite element mesh which follows the evolving form of the melting isotherm throughout the iterations. This method was first introduced for solidification problems by Ettourney and Brown [36]. Figure 16 shows a typical crystal-melt macro-element, where the shape of the meniscus has been calculated at the outset and where the location of the tri-junction is imposed. As an initial guess, one assumes that the interface is flat. The domains Ω_s and Ω_L are then covered by an array of quadrilateral nine-node Lagrangian elements. These nodes are supported by a set of vertical lines. Below the free surface of the

melt, the altitude of the nodes is fixed during the iterations; on the contrary, the altitude of the nodes below the interface and within the crystal will vary with the position of the interface, in order to maintain geometrically well-behaved finite elements throughout the iterations. The various techniques for managing moving meshes automatically have been reviewed in ref. [37].

Let z_i denote the altitude of a node i on the interface. The location of the interface is then fully identified by a vector z containing the z_i 's of all the nodes of Γ . Let k denote a node lying in the melt below node i ; its altitude z_{ik} will then be given by

$$z_{ik} = c_{ik} z_i \quad (69)$$

where c_{ik} is a proportionality factor which is imposed at the outset. The same rule is used for locating the nodes in the crystal.

The concept of deformable mesh has important implications on the finite element discretization of the temperature field, which is now represented, in Ω_L as well as Ω_s , by a sum of the form

$$\tilde{T} = \sum_i \phi_i(z) \quad (70)$$

where we note that the shape functions depend upon the location of Γ through the position of the nodes.

Applying Galerkin's method as we did in Section 4 to the balance equations (63) and (64), one easily obtains

$$\int_{\Omega_s \cup \Omega_L} k \nabla \phi_i \cdot \nabla T \, d\Omega + \int_{\Omega_s} \phi_i v \cdot \nabla T \, d\Omega + \int_{\Gamma} \phi_i q \, d\Sigma = \int_{\Gamma} \phi_i W_\Gamma \, d\Gamma \quad (71)$$

since, from equation (67), we have

$$\int_{\Gamma} \phi_i (q_L + q_s) \, d\Gamma = - \int_{\Gamma} \phi_i W_\Gamma \, d\Gamma. \quad (72)$$

On the outer boundary Σ of Ω , the heat flux density has a representation similar to equation (56) while, along Γ , the nodal temperatures must satisfy equation

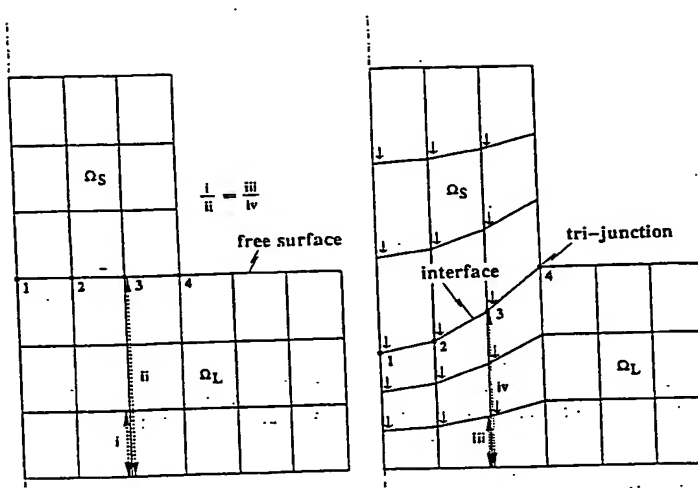


FIG. 16. Typical moving mesh for the crystal-melt macro-element.

(68). In what follows, we will not take convective terms into account; their impact will be discussed in a later paper (see also refs. [15, 17]).

We will now use the same decomposition as in Section 4 and write for the crystal-melt macro-element.

$$\mathbf{T} = [\mathbf{T}^*, \mathbf{T}^+] \quad (73)$$

where \mathbf{T}^* is the vector of internal nodes of the macro-element and \mathbf{T}^+ is the vector of nodal temperatures on its boundary. It is then easy to rewrite equation (71) as follows:

$$\underline{M}^*(z)\mathbf{T}^* + \underline{N}(z)\mathbf{T}^+ = \mathbf{E}^*(z, v_{\text{pul}}) \quad (74)$$

$$\underline{N}^T(z)\mathbf{T}^* + \underline{M}^+(z)\mathbf{T}^+ + \underline{B}^+ \mathbf{q}^+ = \mathbf{E}^+(z, v_{\text{pul}}) \quad (74)$$

where \underline{M}^* , \underline{M}^+ , \underline{N} , \underline{B}^+ and \mathbf{q}^+ are defined as in equations (55) and (57), and where

$$\mathbf{E}^*(z, v_{\text{pul}}) = \left\{ \int_{\Gamma} \phi_{i^*} W_r d\Gamma \right\},$$

$$\mathbf{E}^+(z, v_{\text{pul}}) = \left\{ \int_{\Gamma} \phi_{i^+} W_r d\Gamma \right\}. \quad (75)$$

We observe that the matrices \underline{M}^* , \underline{M}^+ and \underline{N} depend upon the location z of the interface while \mathbf{E}^* and \mathbf{E}^+ also depend upon the pulling rate. For a given value of z and v_{pul} , it is again easy to perform a static condensation and obtain

$$\underline{A}^+(z)\mathbf{T}^+ + \underline{B}^+ \mathbf{q}^+ = \mathbf{C}^+(z, v_{\text{pul}}) \quad (76)$$

where $\underline{A}^+(z)$ is defined as in equation (58) while we have

$$\mathbf{C}^+(z, v_{\text{pul}}) = \mathbf{E}^+(z, v_{\text{pul}}) - \underline{N}^T \underline{M}^{*-1} \mathbf{E}^*(z, v_{\text{pul}}). \quad (77)$$

The vector z is unknown at the outset; the corresponding system of equations is

$$\mathbf{T}^r = \mathbf{T}_i \quad (78)$$

where \mathbf{T}^r is the vector of nodal temperatures along Γ , and \mathbf{T}_i is a vector with all components equal to the nodal temperature at the tri-junction.

5.3. Local iterative scheme

We will show in Section 6 how the calculation of the temperature field and the z vector within the crystal-melt macro-element can be decoupled from the calculations on the rest of the furnace. Let us assume that either the temperature or the heat flux is specified at each node of the boundary of the macro-element. The non-linear system of equations (74) and (78) is then solved by means of Newton-Raphson's method. Let $\mathbf{T}^*, \mathbf{T}^+, \mathbf{q}^+$ and z denote the set of unknowns after a given iteration; the corrections $\delta\mathbf{T}^*$, $\delta\mathbf{T}^+$ and δz are then obtained through the solution of

$$\underline{M}^* \delta\mathbf{T}^* + \underline{N} \delta\mathbf{T}^+ + \delta z \cdot [\nabla, \underline{M}^* \mathbf{T}^* + \nabla, \underline{N} \mathbf{T}^+ - \nabla, \mathbf{E}^*] = \mathbf{E}^* - \underline{M}^* \mathbf{T}^* - \underline{N} \mathbf{T}^+ \quad (79)$$

$$\underline{N}^T \delta\mathbf{T}^* + \underline{M}^+ \delta\mathbf{T}^+ + \delta z \cdot [\nabla, \underline{N}^T \mathbf{T}^+ - \nabla, \mathbf{E}^+] = - \underline{B}^+ \mathbf{q}^+ - \underline{N}^T \mathbf{T}^* - \underline{M}^+ \mathbf{T}^+ + \mathbf{E}^+ \quad (79)$$

$$\delta\mathbf{T}^r = 0. \quad (79)$$

The iterative procedure is interrupted once the magnitude of the right-hand sides in equations (79) lies below a pre-assigned criterion.

In developing equations (79), we have assumed that the pulling rate v_{pul} was known. In Section 6, we will discuss an algorithm where v_{pul} is unknown; it is then necessary to add to both left-hand sides of equations (79) a term of the form:

- (i) $-\delta v_{\text{pul}} \partial \mathbf{E}^* / \partial v_{\text{pul}}$,
- (ii) $-\delta v_{\text{pul}} \partial \mathbf{E}^+ / \partial v_{\text{pul}}$,

respectively, while the equation corresponding to the new unknown v_{pul} states that the tri-junction is at the melting temperature

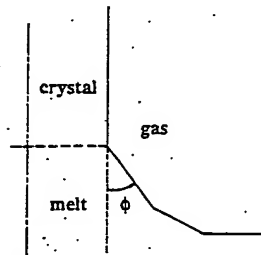


FIG. 17. Fixed wetting angle ϕ between the vertical wall of the crystal and the surface of the melt.

$$T_i = T_m. \quad (80)$$

5.4. Calculation of the meniscus shape

Before closing this section, it should be recalled that, for an accurate calculation of the melting point isotherm and of the heat transfer near the tri-junction, it is necessary to know the shape of the meniscus which links the edge of the crystal and the upper surface of the melt.

An important parameter for calculating the meniscus shape is the angle ϕ shown in Fig. 17 between the vertical surface of the crystal and the surface of the melt. We assume that this wetting angle ϕ is a fixed material property. The latter has been postulated by Bardsley *et al.* [38] (through arguments of thermodynamic equilibrium) and has been verified experimentally by Surek and Chalmers [39] for silicon over a wide range of growth rates. For the case of a crystal obtained by the LEC method, one should also consider a second meniscus at the boundary between the crystal and the upper surface of the boric oxide layer. For this second meniscus, we also assume that the angle of contact can be imposed.

The locations of the melt and encapsulant menisci are governed by the Young-Laplace equation expressing a force balance between surface tension and gravity [40]. The equation is solved at the outset by a decoupled finite element scheme; the shapes of the menisci are left unaffected during the global iterative procedure.

6. GLOBAL SOLUTION

We have shown in earlier sections that, for every kind of macro-element, it is possible to obtain a system of algebraic equations connecting nodal temperatures and heat fluxes along the skeleton. To summarize, let us assume that the puller may be associated with n_r radiative enclosures. For each of these, we obtained in Section 3 a system of the form

$$\mathbf{q}^{(k)} = \underline{F}^{(k)} \mathbf{T}^{(k)4}, \quad 1 \leq k \leq n_r \quad (81)$$

where the full matrix $\underline{F}^{(k)}$ connects the nodal heat fluxes to the fourth power of the nodal temperatures. Let us also consider n_c conductive macro-elements, including the heater as well as the crystal-melt macro-

element. For each of these, we found in Sections 4 and 5 a relationship of the form

$$\underline{A}^{(j)}(z) \mathbf{T}^{(j)} + \underline{B}^{(j)} \mathbf{q}^{(j)} = \underline{C}^{(j)}(z, v_{\text{pul}}, W), \quad 1 \leq j \leq n_c \quad (82)$$

where again $\mathbf{T}^{(j)}$ and $\mathbf{q}^{(j)}$ are the nodal temperatures and heat fluxes on the skeleton part of the boundary of the domain. The dependence of $\underline{A}^{(j)}$ and $\underline{C}^{(j)}$ upon z and v_{pul} only occurs for the crystal-melt macro-element, while W only appears in the macro-element(s) where heat is being dissipated. We note that $\underline{A}^{(j)}$ has a block structure while $\underline{B}^{(j)}$ has a band structure.

Equations (78), which correspond to the unknowns characterizing the position of the interface, must also be considered. Moreover, since we have assumed that the radius of the crystal is fixed at the outset, the pulling rate v_{pul} and the input power W are dependent variables; however, one or the other is assigned as part of the data for a global simulation. The equation corresponding to the remaining unknown is equation (80).

The system (81), (82), (78) and (80) is highly nonlinear, in view of the fourth power of T in equation (82) and the dependence of the various matrix operators upon z . The need for an iterative procedure is obvious. Decoupling is also necessary in view of the size of the system. On the basis of $\mathbf{T}^{(j)}$ in equation (82), it is possible to recover the temperature field in any macro-element by means of an equation of the form

$$\underline{M}^{*(j)}(z) \mathbf{T}^{*(j)} + \underline{N}^{(j)}(z) \mathbf{T}^{(j)} = \underline{E}^{*(j)}(z, v_{\text{pul}}, W). \quad (83)$$

6.1. Skeleton equations

Before describing the global iterative algorithm, let us assume that z , v_{pul} and W are known, and let us show how it is then possible to calculate the temperature field on the skeleton, without using equations (78) and (80). The term $\underline{B}^{(j)} \mathbf{q}^{(j)}$ in equation (82) stands for generalized nodal heat fluxes $\mathbf{Q}^{(j)}$ along the boundary of the macro-element (see equation (57)). Along the common border of two conductive macro-elements, such nodal heat fluxes are of opposite sign. They can thus be easily eliminated from the global system simply by adding the appropriate equations of the form of equation (82) along the common borders. It is thus possible to obtain a system of the form

$$\underline{A}(z) \mathbf{T}^* + \underline{B} \mathbf{q}^* = \underline{C}(z, v_{\text{pul}}, W) \quad (84)$$

which relates the nodal temperatures \mathbf{T}^* and the radiative heat fluxes \mathbf{q}^* along the skeleton. We note that the matrix \underline{B} is rectangular since the nodal heat fluxes have been eliminated along the common border of adjacent conductive macro-elements. In the same way, we write equation (81) as follows:

$$\mathbf{q}^* = \underline{F} \mathbf{T}^* \quad (85)$$

where \underline{F} is also rectangular.

At geometrical corners of radiative enclosures, we had been led to identify a different nodal heat flux on both sides of the corner, while the associated tem-

perature is obviously unique. For handling the system (84) and (85), we have found it easier to also define two temperatures at geometrical corners in order to have the same number of nodal heat fluxes and nodal temperatures. The equality of both temperatures at the nodes is then imposed as an additional constraint. Introducing equation (85) in equation (84), we obtain

$$\underline{A}(z)T^* + \underline{B}FT^* = \underline{C}(z, v_{pul}, W). \quad (86)$$

Assuming again that z , v_{pul} and W are known, this is a non-linear system in terms of the skeleton temperatures. It is solved by means of the modified Newton's method (also called Newton-Richardson [41]). A LU factorization of the Jacobian matrix is executed by means of an algorithm which is well suited for hollow matrices with irregular structure [42]. Having solved equation (86), we obtain the set of nodal temperatures along the skeleton. From these, it is then possible to calculate the nodal temperatures inside macro-elements by means of equation (83), while radiative heat fluxes can be retrieved from equation (85).

6.2. Global algorithm: W imposed

Let us first assume that, for a given crystal radius, the input power W is imposed while the corresponding pulling rate is unknown. For solving the system, we use a decoupled iterative procedure which is described as follows. Let z_n and v_{pul}^n denote the corresponding values of z and v_{pul} after iteration n ; typically, we will assume that v_{pul}^0 vanishes while z_0 corresponds to a horizontal interface.

On this basis, we solve equation (86) and obtain a set of nodal temperatures T_{n+1}^* along the skeleton from which we calculate, with the help of equation (85), the nodal heat fluxes q_{n+1}^* .

Next, we perform a decoupled calculation on the crystal-melt macro-element for calculating z_{n+1} and v_{pul}^{n+1} . With that objective in mind, we solve the system of equations (74) and (78) with v_{pul} as an additional unknown and equation (80) as an additional constraint; as boundary conditions, we use T_{n+1}^* along the melt-crucible interface, and q_{n+1}^* along the surface of the melt and the wall of the crystal. The new values of z_{n+1} and v_{pul}^{n+1} are then used for recalculating the matrices in equation (86). The iterations are pursued until convergence criteria for T^* , z and v_{pul} are satisfied.

The above decoupled iterative procedure converges in general, but can lead to unexpected and often unrealistic results. Indeed, it is found in practice as well as in theory that a slight modification of the power input can lead to important variations of the pulling rate for keeping the crystal diameter constant. Since the power input cannot be precisely measured on industrial pullers, one can easily obtain unrealistic huge values of the pulling rate.

6.3. Global algorithm: v_{pul} imposed

In view of the above considerations, we found it much more efficient to impose the pulling rate, which

is a control variable in industrial growth, and to calculate the necessary power input. The decoupled iterative procedure may be described as follows. Let z_n and W_n denote the corresponding values of z and W after iteration n ; we will assume for W_0 a first guess based on a rough estimate. We solve equation (86) for T^* and W , with equation (80) as an additional constraint, i.e. we select the power input such that the temperature at the tri-junction is precisely the melting temperature. We obtain T_{n+1}^* and q_{n+1}^* and then perform a decoupled calculation on the crystal-melt macro-element for calculating z_{n+1} , while v_{pul} is fixed. The boundary conditions for the decoupled problem are the same as in Section 6.2, except that constraint (80) does not apply at this stage. The iterations are pursued until convergence criteria for T^* , z and W are satisfied.

The stability properties of the algorithm where v_{pul} is imposed are remarkable, and definitely better than those found when W is imposed. In practical applications, a relative accuracy of 1% is obtained with six global iterations. The solution of equation (86) requires some four iterations for the first resolution and only one for the next iterations, while equations (74) and (78) require some four iterations.

7. EVALUATION OF THERMAL STRESSES

Performing the fully coupled calculations of Section 6, we are able to obtain an accurate temperature field and the shape of the liquid-solid interface during growth. We may thus calculate the stress field without any arbitrary simplifying assumptions on the shape of the crystal and the temperature field. A realistic calculation of the stress field would in turn require a continuum model taking into account the material properties of the crystal near the melting temperature. However, in view of the lack of material data at such high temperatures for the metals which we have considered, we have been led to formulate the following hypotheses:

- (i) the crystal is an isotropic linearly elastic solid and the stress field is axisymmetric; deformations are reversible and plasticity and creep are not taken into account;
- (ii) the thermal field is decoupled from the stress field;
- (iii) the material properties of the crystal (Young's modulus, Poisson's ratio, thermal expansion coefficient) are temperature independent;
- (iv) the crystal is free of surface forces;
- (v) the crystal is stress free under a uniform temperature field.

The finite element calculation of thermal stresses under such conditions is straightforward (see, e.g. ref. [31]). A quantity of interest for evaluating the generation of dislocations is the Mises invariant which is defined as follows:

$$S_M = [(S_1 - S_2)^2 + (S_2 - S_3)^2 + (S_3 - S_1)^2]^{1/2} \quad (87)$$

where S_1 , S_2 and S_3 are the principal stresses. It is generally accepted that plastic deformations occur where S_M reaches a critical value.

8. RESULTS

In the present section, we wish to demonstrate the efficiency of our numerical method through an analysis of two typical calculations. The first set of results corresponds to a Czochralski furnace for the growth of germanium crystals; we will show that, for calculating the growth of a crystal with fixed radius, it is much more efficient to impose the pulling rate than the power input. Our second example refers to the LEC growth of a gallium arsenide crystal; we will find that the semi-transparent properties of the oxide layer have a major impact upon various aspects of the solution.

8.1. Germanium growth

A typical furnace for growing germanium crystals is shown in Fig. 18; for the sake of clarity, a different scale is used in the radial and axial directions. In the present example, the crystal diameter is 10 cm, its length is 20 cm, and the total weight of metal is 30 kg. The meniscus near the tri-junction has little impact in the present calculation and has been neglected. The germanium melting temperature is 1211 K; the other physical properties of the materials are given in Table 1.

It should be noted that some thermal properties, and the emissivity in particular, are highly dependent upon the grade and the surface state of the material. This explains why some values for the same material appear to be different for both germanium and gallium arsenide furnaces.

The finite element mesh used for the calculations is shown on the left part of Fig. 19. The global mesh contains 965 biquadratic elements and 4317 nodes. The skeleton supports 792 nodes. A typical growth rate for the process is 3 cm h^{-1} ; the corresponding isotherms are shown on the right part of Fig. 19. The crystal is slightly concave at the interface, with a deflection of 0.6 mm. The necessary power in the heater is 24.5 kW. To obtain the solution, we have performed six global iterations with adjustment of the power input; for each global iteration, we needed three inner iterations for locating the interface; the

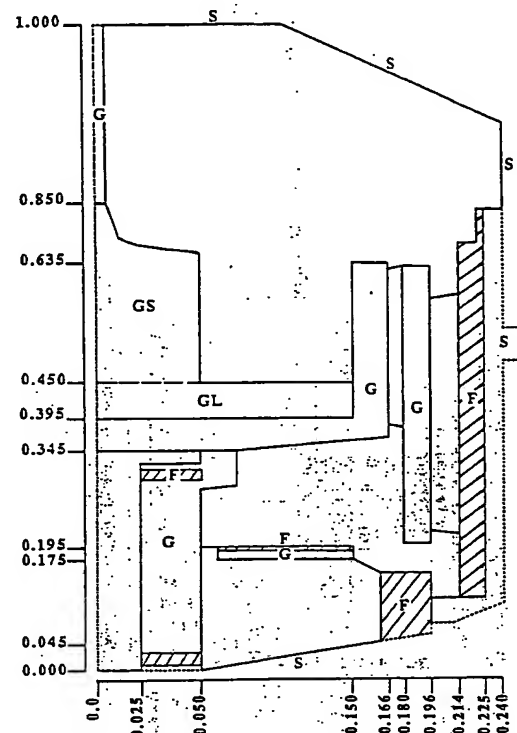


FIG. 18. Draft of the germanium furnace used for the simulations (radial axis is dilated).

convergence criterion was 10^{-6} K for the temperature field and 10^{-6} m for the position of the interface.

An interesting problem is to determine the maximum value of the growth rate for a given process stage. In view of the high non-linearity of the problem, the pulling rate can only be increased in this case by a series of increments (the convergence of the iterative procedure could not be obtained otherwise). Let us examine in Fig. 20 the isotherms which have been obtained for values of v_{pul} equal respectively to 4.2 , 4.4 and 4.6 cm h^{-1} ; for this last value, the input power has decreased to 24.05 kW . From Fig. 20, we find that the maximum pulling rate is 4.4 cm h^{-1} since, at 4.6 cm h^{-1} , the melting point isotherm extends within the melt around the crystal; it is therefore impossible to maintain a crystal of constant radius. Even at 4.4 cm h^{-1} ,

Table 1. Thermal properties of the materials used in the germanium furnace.

Material	Symbol in Fig. 18	Conductivity ($\text{W m}^{-1} \text{K}^{-1}$)	Emissivity
Solid germanium	GS	25.0	0.55
Liquid germanium	GL	75.0	0.20
Graphite	G	60.0	0.81
Steel	S	30.0	0.30
Insulating material	F	0.07	—

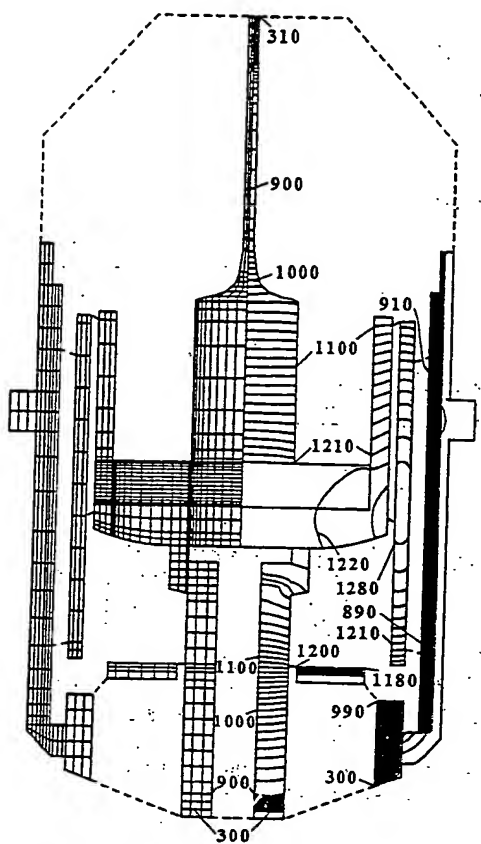


FIG. 19. Sketch of the germanium furnace with finite element mesh (left) and isotherms separated by steps of 10 K (right).

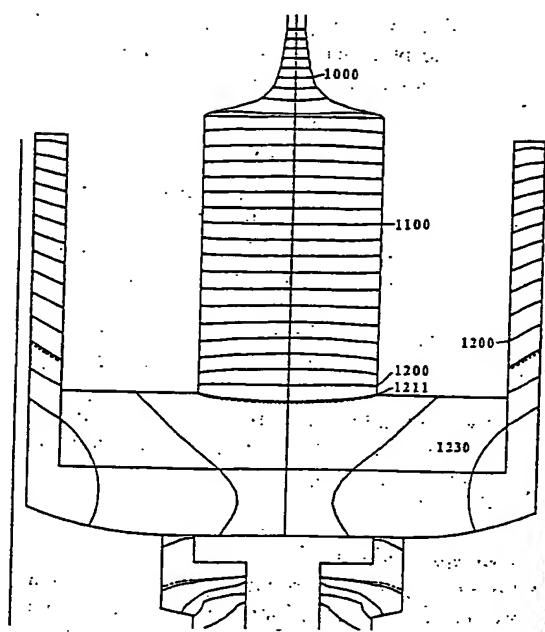


FIG. 21. Isotherms in the germanium furnace separated by steps of 10 K for an imposed growth rate of 1.4 cm h^{-1} .

h^{-1} , we find that the melting point isotherm is tangent to the surface of the melt; such a temperature distribution could make it difficult to control the diameter of the crystal. Quite clearly, the effect of increasing the pulling rate is to produce a concavity of the crystal at the interface, with a deflection of 8.6 mm at a growth rate of 4.4 cm h^{-1} . To the contrary, a low pulling rate of 1.4 cm h^{-1} leads to a convex crystal, with a deflection of 6.9 mm, as we may see in Fig. 21; the input power is then 25.0 kW.

It is clear that slight changes of the input power (between 24 and 25 kW) are associated with major modifications of the pulling rate (between 4.6 and 1.4 cm h^{-1}) for keeping the crystal diameter constant; it was therefore advisable to use the pulling rate rather than the power input as the control parameter for the calculations. Let us however analyse the case where the power input is imposed at a value of 26 kW, with the result at 25 kW as a first guess. With such a jump in the input power, it is impossible to apply in a straightforward manner the method of Section 6, because the initial guess lies too far from the solution. However, convergence can be obtained by applying a sub-relaxation algorithm, i.e. by imposing as constraint on the interface. Instead of equation (80), we use

$$T_{n+1} = (1-\alpha)T_n + \alpha T_n \quad (88)$$

where α is a sub-relaxation parameter while n refers

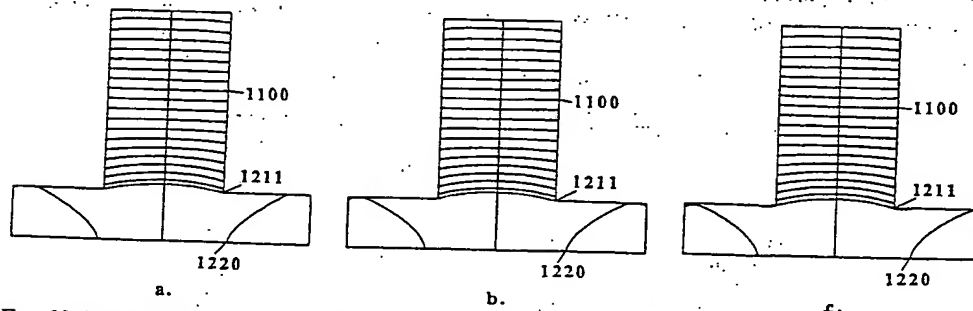


FIG. 20. Isotherms separated by steps of 10 K in the germanium melt and crystal, for different growth rates: (a) 4.2 cm h^{-1} ; (b) 4.4 cm h^{-1} ; (c) 4.6 cm h^{-1} .

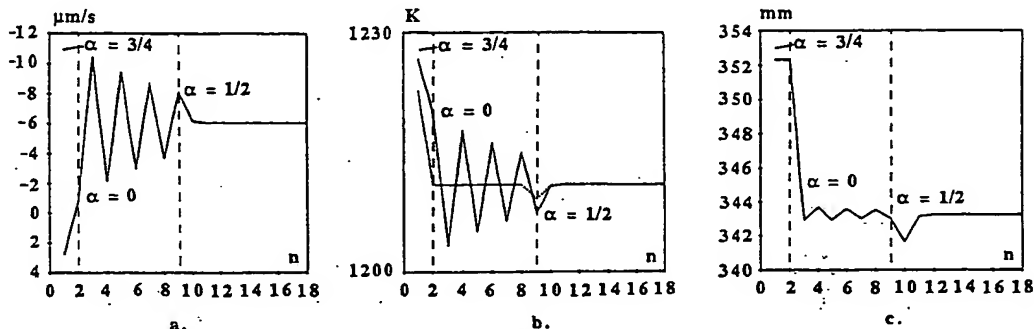


FIG. 22. Evolution of growth rate (a), temperature at the tri-junction (b) and position of the interface along the axis of symmetry (c) during the numerical iterations when the power input is imposed.

to the n th global iteration. We found that an initial value of 0.75 for α was suitable, in this case, for controlling the oscillatory behaviour of the iterations. Figure 22 shows the evolution of the pulling rate v_{pal} (a), the imposed interface temperature T_i (b) (see equation (78)), and the axial interface position (c) during successive iterations. Having started the procedure with $\alpha = 0.75$, we select the value 0 which immediately generates oscillations. A strong damping is observed once the value of 0.5 is selected. The final solution is shown in Fig. 23: the crystal becomes much more convex at the interface (with a deflection of 22 mm) while the pulling rate reaches a *negative value* of -2.2 cm h^{-1} . Since the power input is too high, we are actually melting the crystal by pushing it into the melt: the natural issue would be to grow a crystal of smaller radius.

8.2. Gallium arsenide growth

As a second example, we will calculate the LEC growth of a gallium arsenide crystal. The liquid boric oxide layer, which is used to prevent evaporation of the volatile component, can be considered as transparent for a range of wavelengths and opaque for the others. It has been shown in ref. [43] that transparency occurs for wavelengths lower than about $2.3 \mu\text{m}$.

As explained in Section 3.4, we will consider two different radiative enclosures, corresponding to both ranges of wavelengths. For the first enclosure, the function $\gamma_A(T)$ defined by equations (2), (3) and (4) is given by

$$\gamma_{A_1} = F(2.3 * 1511) - F(0) = 0.4 \quad (89)$$

while for the second enclosure, we have

$$\gamma_{A_2} = F(\infty) - F(2.3 * 1511) = 0.6. \quad (90)$$

We wish to investigate the effect of the value of γ_{A_2} upon the global solution. Recall that $\gamma_{A_2} = 0$ for a fully transparent medium, while $\gamma_{A_2} = 1$ when it is fully opaque.

The physical properties adopted for the present simulation are given in Table 2. Note that the melting temperature of gallium arsenide is 1511 K. The geometry of the furnace and the finite element mesh used for the simulation are shown in Fig. 1. The crystal diameter is 6.4 cm (2.5 in.), the length is 5.2 cm and the total weight (melt and crystal) is 4 kg.

A global view of the isotherms for the case $\gamma_{A_2} = 0.5$ and a pulling rate of 1 cm h^{-1} is given in Fig. 24. We note that, for the present problem, we have calculated the shape of the meniscus for the surface of the melt and of the oxide layer.

In Fig. 25, we show the isotherms and the contour lines of the Mises invariant S_M defined by equation (87), for values of γ_{A_2} respectively equal to 0, 0.25, 0.50, 0.75 and 1, and for the same pulling rate of 1 cm h^{-1} . It is clear that the degree of opacity of the oxide layer has a major impact upon the process. In particular, in going from the transparent case at $\gamma_{A_2} = 0$ up to the opaque situation at $\gamma_{A_2} = 1$, we find that:

- (i) the crystal, which is initially concave at the interface, becomes convex;

Table 2. Thermal properties of the materials used in the gallium arsenide furnace

Material	Symbol	Conductivity ($\text{W m}^{-1} \text{K}^{-1}$)	Emissivity
Solid gallium arsenide	Ga As S	7.2	0.36
Liquid gallium arsenide	Ga As L	17.1	0.36
Graphite	G	42.0	0.64
Quartz	Q	3.0	0.5
Steel	S	27.2	0.45
Boric oxide	B	1.7	0.5
Graphite felt	F	1.0	—

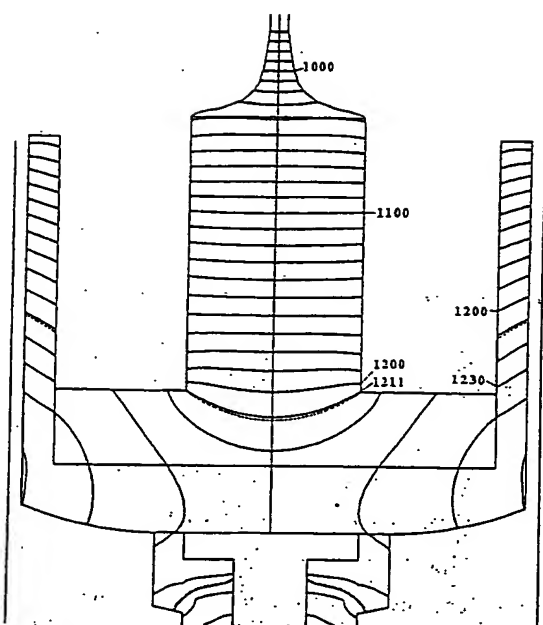


FIG. 23. Isotherms in the germanium furnace separated by steps of 10 K for an imposed power input of 26 kW.

- (ii) the vertical temperature gradient in the melt decreases, while the horizontal temperature gradient on the surface of the melt increases;
- (iii) the vertical temperature gradient in the oxide layer strongly increases;

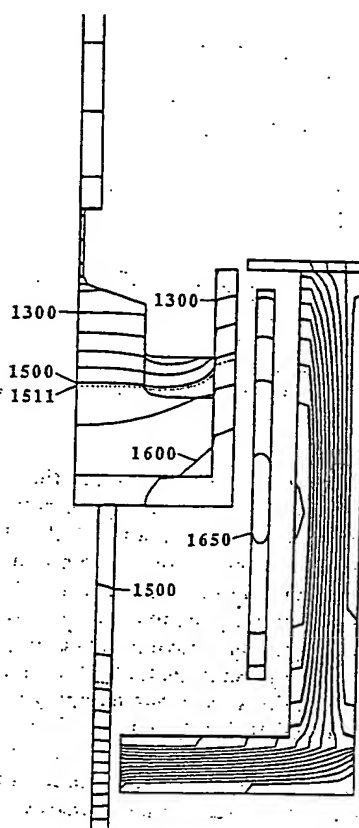


FIG. 24. Isotherms in the LEC furnace for $\gamma_{A_2} = 0.5$ and a pulling rate of 1 cm h^{-1} , separated by steps of 50 K.

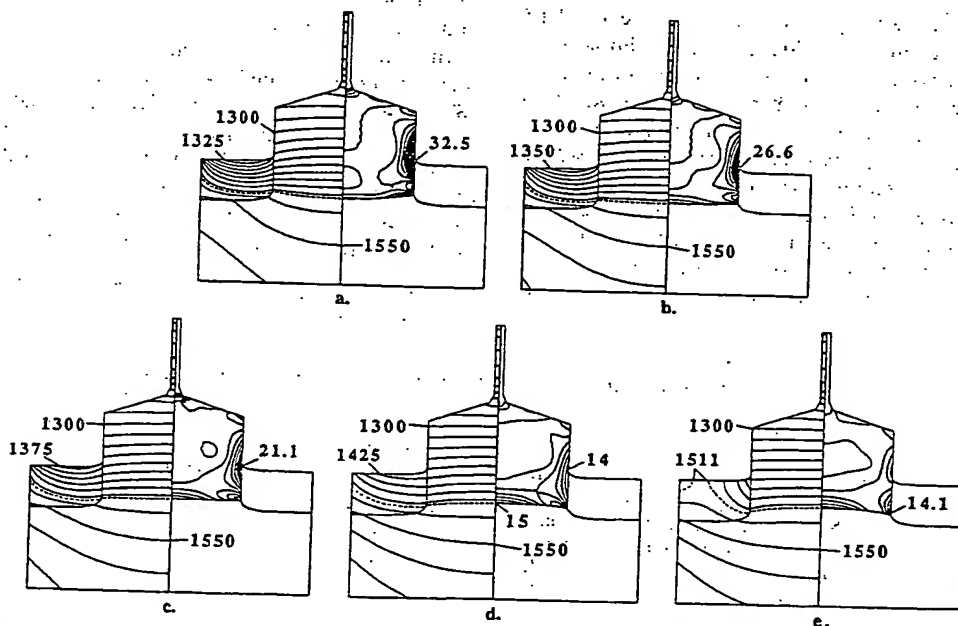


Fig. 25. Isotherms separated by steps of 25 K, and iso-stress lines separated by steps of 2 MPa, for values of γ_{A_2} equal to 1.0 (a), 0.75 (b), 0.5 (c), 0.25 (d) and 0.0 (e) and the same pulling rate of 1 cm h^{-1} .

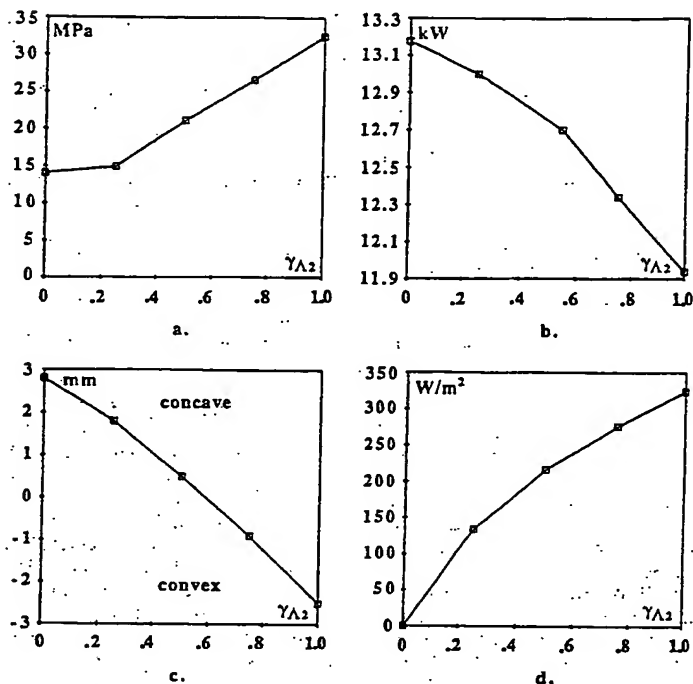


FIG. 26. Evolution of the maximal stress (von Mises) (a), the power dissipated in the heater (b), the deflection of the interface (c) and the flux leaving the top of the boric oxide layer (d) as a function of the opacity coefficient γ_{A2} .

(iv) the stress level increases along the edge of the crystal;

(v) the stress level along the axis of symmetry decreases near the interface.

The sensitivity of the system is summarized in Fig. 26, showing the dependence of some important output parameters upon γ_{A2} , i.e. the maximum value of S_M , the power input, the deflection of the interface and the total heat flux leaving the upper surface of the boric oxide layer. We note that all these parameters depend appreciably upon the radiative properties of the encapsulant.

9. CONCLUSIONS

The accurate prediction of the shape of the melt-crystal interface and the temperature field within the crystal requires a global modelling of heat transfer in the entire furnace. We have presented a self-contained model where, for any given geometry, the input parameters are limited to the coolant temperature, the power input or the pulling rate, and the radius of the crystal. Radiative exchanges are accurately calculated since viewed and hidden parts of the enclosures are taken into account. The effect of melt convection will be analysed in a further publication.

We have demonstrated, on the basis of simulations of germanium and gallium arsenide growth, that our model is relevant for evaluating the sensitivity of the

final product upon material and geometrical parameters. It is a valuable tool for growth control and furnace design.

Acknowledgements—This research was supported in part by the Belgian IRSIA project No. 4866 and in part by the European ESPRIT project No. 1128. The authors wish to acknowledge the following companies: Metallurgie-Hoboken-Overpelt, in Belgium, Wacker-Chemtronic, in West Germany, and the LEP (Laboratoire d'Electronique de Philips), in France, for a long standing and stimulating scientific collaboration.

REFERENCES

1. N. Kobayashi, Heat transfer in Czochralski crystal growth. In *Preparation and Properties of Solid State Materials* (Edited by W. R. Wilcox), Vol 6. Marcel Dekker, New York (1981).
2. J. J. Derby, L. N. Atherton, P. D. Thomas and R. A. Brown, Finite element methods for analysis of the dynamics and control of Czochralski crystal growth, *J. Sci. Comput.* 2, 297 (1987).
3. J. J. Derby, R. A. Brown, F. T. Geyling, A. S. Jordan and G. A. Nikolakopoulou, Finite element analysis of a thermal-capillary model for liquid encapsulated Czochralski growth, *J. Electrochem. Soc.* 132, 470 (1985).
4. J. J. Derby and R. A. Brown, On the quasi-steady-state assumption in modelling batchwise Czochralski growth, *J. Crystal Growth* 87, 251 (1988).
5. J. J. Derby and R. A. Brown, Thermal-capillary analysis of Czochralski and liquid encapsulated Czochralski crystal growth—I. Steady-state simulation, *J. Crystal Growth* 74, 605 (1986).
6. J. J. Derby and R. A. Brown, Thermal-capillary analysis

of Czochralski and liquid encapsulated Czochralski crystal growth—II. Processing strategies, *J. Crystal Growth* 75, 227 (1986).

7. L. J. Atherton, J. J. Derby and R. A. Brown, Radiative heat exchange in Czochralski crystal growth, *J. Crystal Growth* 84, 57 (1987).
8. R. K. Srivastava, P. A. Ramachandran and M. P. Dudukovic, Interface shape in Czochralski grown crystals: effect of conduction and radiation, *J. Crystal Growth* 73, 487 (1985).
9. S. Motakef and A. F. Witt, Thermoelastic analysis of GaAs in LEC growth configuration—I. Effect of liquid encapsulant on thermal processes, *J. Crystal Growth* 80, 37 (1987).
10. S. Motakef, Effect of natural convection and thermal transparency of liquid encapsulant on thermal stresses during LEC growth of GaAs, *Int. J. Heat Mass Transfer* 30, 1487 (1987).
11. S. Motakef, Thermoelastic analysis of GaAs in LEC growth configuration—II. Temporal evolution of the stress field, *J. Crystal Growth* 88, 341 (1988).
12. P. Wouters, Simulation numérique des échanges thermiques et application à la croissance des cristaux semi-conducteurs, Ph.D. Dissertation, Université Catholique de Louvain, Belgium (1985).
13. F. Dupret, Y. Ryckmans, P. Wouters and M. J. Crochet, Numerical calculation of the global heat transfer in a Czochralski furnace, *J. Crystal Growth* 79, 84 (1986).
14. F. Dupret, P. Nicodème and Y. Ryckmans, A numerical method for reducing stress level in GaAs crystals, *J. Crystal Growth* 97, 162 (1989).
15. F. Dupret, Y. Ryckmans, P. Wouters and M. J. Crochet, Global finite element calculation of the Czochralski growth, *Proc. Sixth Int. Symp. on Finite Element Methods in Flow Problems*, Antibes, France, p. 267 (June 1986).
16. P. Nicodème, F. Dupret and M. J. Crochet, Effect of geometrical parameters upon the LEC growth of GaAs crystals, *Proc. 5th Int. Conf. on Semi-insulating III-V Materials* (Edited by G. Grossman and L. Ledebo), p. 465. Adam Hilger (June 1988).
17. P. Nicodème, F. Dupret, M. J. Crochet, J. P. Farges and G. Nagel, Numerical simulation of heat transfer in LEC growth of gallium arsenide, *Proc. 5th Int. Conf. on Semi-insulating III-V Materials* (Edited by G. Grossman and L. Ledebo), p. 471. Adam Hilger (June 1988).
18. J. R. Howell, Application of Monte Carlo to heat transfer problems. In *Advances in Heat Transfer* (Edited by J. P. Hartnett and T. F. Irvine), Vol. 5 (1968).
19. R. Siegel and J. Howell, *Thermal Radiation Heat Transfer* (2nd Edn). McGraw-Hill, New York (1981).
20. B. Gebhart, Unified treatment for thermal radiation transfer processes—gray, diffuse radiators and absorbers, Paper No. 57-A-34, ASME (1957).
21. H. C. Hottel, Radiant-heat transmission. In *Heat Transmission* (Edited by W. H. McAdams), Chap. 4. McGraw-Hill, New York (1954).
22. M. Jakob, *Heat Transfer*, Vol. II. Wiley, New York (1957).
23. G. Poljak, Analysis of heat interchange by radiation between diffuse surfaces, *Tech. Phys. USSR* 1(5, 6), 555 (1935).
24. F. B. Hildebrand, *Methods of Applied Mathematics*. Prentice-Hall, Englewood Cliffs, New Jersey (1952, 1965).
25. C. Garot and P. Gendre, Computation of view factors used in radiant energy exchanges in axisymmetric geometry. In *Numerical Methods in Thermal Problems*. Pineridge Press, Swansea (1979).
26. E. Billig, Growth of monocrystals of germanium from an undercooled melt, *Proc. R. Soc. London A235*, 37 (1956).
27. P. Penning, Generation of imperfections in germanium crystals by thermal strain, *Philips Res. Report* 13, 79 (1958).
28. N. Kobayashi and T. Iwaki, A thermoelastic analysis of the thermal stress produced in a semi-infinite cylindrical single crystal during the Czochralski growth, *J. Crystal Growth* 73, 96 (1985).
29. A. S. Jordán, A. R. Caruso, A. R. Von Neida and J. W. Nielsen, A comparative study of thermal stress induced dislocation generation in pulled GaAs, InP, and Si crystals, *J. Appl. Phys.* 52, 3331 (1981).
30. A. S. Jordán, A. R. Caruso, A. R. Von Neida and J. W. Nielsen, A thermoelastic analysis of dislocation generation in pulled GaAs crystals, *Bell System Tech. J.* 59, 593 (1980).
31. M. Duseaux, Température profile and thermal stress calculations in GaAs crystals growing from the melt, *J. Crystal Growth* 61, 576 (1983).
32. C. E. Schvezov, I. V. Samarasekera and F. Weinberg, Mathematical modelling of the liquid encapsulated Czochralski growth of gallium arsenide—II. Stress model, *J. Crystal Growth* 84, 219 (1987).
33. M. J. Crochet, P. J. Wouters, F. T. Geyling and A. S. Jordan, Finite element simulation of Czochralski bulk flow, *J. Crystal Growth* 65, 153 (1983).
34. N. Kobayashi and T. Arizumi, The numerical analysis of the solid-liquid interface shape during the crystal growth by the Cz. method—I and II, *Jap. J. Appl. Phys.* 9, 361, 1255 (1970).
35. P. Wouters, J. J. Van Schaftingen, M. J. Crochet and F. T. Geyling, Numerical simulation of the horizontal Bridgman growth—III. Calculation of the interface, *Int. J. Numer. Meth. Fluids* 7, 131 (1987).
36. H. M. Ettourney and R. A. Brown, Finite-element methods for steady solidification problems, *J. Comput. Phys.* 49, 118 (1983).
37. D. R. Lynch, Unified approach to simulation on deforming elements with application to phase change problems, *J. Comput. Phys.* 47, 387 (1982).
38. W. Bardsley, F. C. Franck, G. W. Green and D. T. J. Hurle, The meniscus in Czochralski growth, *J. Crystal Growth* 23, 341 (1974).
39. T. Surek and B. Chalmers, The direction of growth of the surface of a crystal in contact with its melt, *J. Crystal Growth* 29, 1 (1975).
40. D. T. J. Hurle, Analytical representation of the shape of the meniscus in Czochralski growth, *J. Crystal Growth* 63, 13 (1983).
41. J. M. Ortega and W. C. Rheinboldt, Iterative solution of nonlinear equations in several variables. In *Computer Science and Applied Mathematics*. Academic Press, New York (1970).
42. A. Georges and J. Liu, *Computer Solution of Large Sparse Positive Definite Systems*. Prentice-Hall, Englewood Cliffs, New Jersey (1981).
43. A. G. Ostrogorsky, K. H. Yao and A. F. Witt, Infrared absorbance of B_2O_3 at temperatures to 1250°C, *J. Crystal Growth* 84, 460 (1987).

UN MODELE GLOBAL POUR CALCULER LES TRANSFERTS DE CHALEUR DANS LES FOUS DE TIRAGE DE CRISTAUX

Résumé—Pour prédire en cours de croissance le champ de température dans un cristal, ainsi que la forme de l'interface qui sépare le bain de ce cristal, il faut déterminer avec précision les transferts de chaleur qui ont lieu dans le four tout entier. La résolution de ce problème est très complexe, car il y a lieu de calculer précisément à la fois les échanges radiatifs entre les différentes surfaces et les transferts par conduction à l'intérieur des constituants du four. Les échanges radiatifs sont évalués sur base de l'hypothèse que la radiation est diffuse et se fait en surface tandis que les calculs se font par la méthode de discréétisation de Galerkin, à l'aide d'un algorithme spécifique de calcul des vues et cachées. Le modèle a été étendu pour prendre en compte le caractère semi-transparent de certains matériaux. La forme de l'interface liquide-solide est une inconnue du problème, que l'on calcule en l'assimilant à l'isotherme de fusion. Des exemples de fours de tirage de germanium et d'arsénure de gallium sont analysés, ce qui permet d'illustrer la puissance de la méthode.

EIN GLOBALES MODELL FÜR DEN WÄRMETRANSPORT IN ÖFEN FÜR DIE KRISTALLZÜCHTUNG

Zusammenfassung—Eine quantitative Berechnung des Temperaturfeldes und der Position der Kristalloberfläche beim Wachstum erfordert eine genaue Kenntnis der Wärmetransportvorgänge im gesamten Ofen. Dieses Problem ist äußerst komplex, da es eine exakte Berechnung der Strahlung zwischen den verschiedenen Oberflächen und der Wärmeleitung in den einzelnen Komponenten erfordert. Der Strahlungswärmeaustausch wird unter Annahme von diffusen grauen Oberflächen berechnet. Hierzu wird ein besonderer Algorithmus zusammen mit einer Diskretisierung nach Galerkin verwendet. Dieses Modell wird erweitert, um auch halbdurchlässige Materialien einzubeziehen zu können. Die Form der Flüssigkeits/Feststoff-Grenzfläche ist eine Problemvariable—sie wird in Form der Schmelzisothermen berechnet. Die Wirksamkeit des Verfahrens wird anhand von Beispielen für Germanium- und Gallium-Arsenid-Öfen gezeigt.

МОДЕЛИРОВАНИЕ ТЕПЛОПЕРЕНОСА ПРИ РОСТЕ КРИСТАЛЛОВ В ЕМКОСТИ

Аннотация—Для количественного определения теплового поля и положения границы раздела расплав—кристалл в процессе роста необходимы точные данные по теплопереносу во всей емкости. Эта задача весьма сложна, так как связана с точным расчетом переноса излучения между различными поверхностями и теплопроводностью во всех частях системы. Лучистый теплообмен рассчитывается в приближении диффузно-серых поверхностей и с использованием алгоритма видимой и скрытой частей, а также метода Галеркина. Модель обобщена на учет полупрозрачных материалов. Форма границы раздела жидкость—твердое тело является переменной величиной этой задачи и определяется как изотерма плавления. Анализ процессов для арсенидов германия и галлия подтвердил эффективность метода.

**This Page is Inserted by IFW Indexing and Scanning
Operations and is not part of the Official Record**

BEST AVAILABLE IMAGES

Defective images within this document are accurate representations of the original documents submitted by the applicant.

Defects in the images include but are not limited to the items checked:

- BLACK BORDERS**
- IMAGE CUT OFF AT TOP, BOTTOM OR SIDES**
- FADED TEXT OR DRAWING**
- BLURRED OR ILLEGIBLE TEXT OR DRAWING**
- SKEWED/SLANTED IMAGES**
- COLOR OR BLACK AND WHITE PHOTOGRAPHS**
- GRAY SCALE DOCUMENTS**
- LINES OR MARKS ON ORIGINAL DOCUMENT**
- REFERENCE(S) OR EXHIBIT(S) SUBMITTED ARE POOR QUALITY**
- OTHER:** _____

IMAGES ARE BEST AVAILABLE COPY.

As rescanning these documents will not correct the image problems checked, please do not report these problems to the IFW Image Problem Mailbox.